

The Mass of the Black Hole in LMC X-3[†]

Jerome A. Orosz

Department of Astronomy, San Diego State University, 5500 Campanile Drive, San Diego, CA 92182-1221
 orosz@sciences.sdsu.edu

James F. Steiner, Jeffrey E. McClintock

Harvard-Smithsonian Center for Astrophysics, 60 Garden Street, Cambridge, MA 02138
 jsteiner@cfa.harvard.edu, jem@cfa.harvard.edu

Michelle M. Buxton, Charles D. Bailyn

Department of Astronomy, Yale University, PO Box 208101, New Haven, CT 06520-8101
 michelle.buxton@yale.edu, charles.bailyn@yale.edu

Danny Steeghs

Department of Physics, University of Warwick, Coventry, CV4 7AL, UK and Harvard-Smithsonian Center for Astrophysics, 60 Garden Street, Cambridge, MA 02138
 D.T.H.Steeghs@warwick.ac.uk

Alec Guberman

Byram Hills High School, 12 Tripp Lane, Armonk, NY 10504 and Department of Physics and Astronomy, Stony Brook University, Stony Brook, NY 11794-3800
 alec.guberman@stonybrook.edu
 and

Manuel A. P. Torres

SRON Netherlands Institute for Space Research, Sorbonnelaan 2, 3584 CA Utrecht, the Netherlands and Harvard-Smithsonian Center for Astrophysics, 60 Garden Street, Cambridge, MA 02138
 M.Torres@sron.nl

ABSTRACT

We analyze a large set of new and archival photometric and spectroscopic observations of LMC X-3 to arrive at a self-consistent dynamical model for the system. Using echelle spectra obtained with the MIKE instrument on the 6.5m Magellan Clay telescope and the UVES instrument on the second 8.2m Very Large Telescope we find a velocity semi-amplitude for the secondary star of $K_2 = 241.1 \pm 6.2 \text{ km s}^{-1}$, where the uncertainty includes an estimate of the systematic error caused by X-ray heating. Using the spectra, we also find a projected rotational velocity of $V_{\text{rot}} \sin i = 118.5 \pm 6.6 \text{ km s}^{-1}$. From an analysis of archival *B* and *V* light curves as well as new *B* and *V* light curves from the SMARTS 1.3m telescope, we find an inclination of $i = 69.84 \pm 0.37^\circ$ for models that do not include X-ray heating and an inclination of $i = 69.24 \pm 0.72^\circ$ for models that incorporate X-ray heating. Adopting the latter inclination measurement, we find masses of $3.63 \pm 0.57 M_\odot$ and $6.98 \pm 0.56 M_\odot$ for the companion star and the black hole, respectively. We briefly compare our results with earlier work and discuss some of their implications.

1. Introduction

LMC X-3 was the second black hole, after Cygnus X-1, to be established via dynamical observations (Cowley et al. 1983). The large mass function of the host binary, $f(M) = 2.3 \pm 0.3 M_\odot$, the absence of X-ray eclipses, and the estimated mass of the B3 V secondary ($4 - 8 M_\odot$) allowed Cowley et al. to conclude that “the most probable mass” of the black hole is $M \sim 9M_\odot$, with a plausible lower limit of $M > 7 M_\odot$. A subsequent study of the 1.7-day optical light curve constrained the inclination i to lie in the range $\sim 64^\circ$ to 70° , and it also provided a firm lower limit on the mass of the primary, $M > 3.5 M_\odot$ (Kuiper et al. 1988), thereby confirming that it is indeed a black hole (e.g., Kalogera & Baym 1996). Recently, in the context of a far-UV study of LMC X-3 (Song et al. 2010), and using much of the data discussed herein, we reported a precise ephemeris and radial velocity amplitude for the secondary.

It is a challenge to establish a reliable dynamical model of the LMC X-3 system because both the optical counterpart and the X-ray source are highly variable. In addition to the ≈ 0.15 mag ellipsoidal variations (Kuiper et al. 1988), the optical flux varies chaotically by up to ≈ 1 mag (Brocksopp et al. 2001), while the *RXTE* PCA shows that the X-ray luminosity ranges over a factor of at least 2,500 (Smale & Boyd 2012).

Furthermore, the optical variability (which is most relevant for a dynamical study) is not simply slaved to the X-ray variability as it is in most transient black hole binaries: In a typical transient system, the optical emission is generated directly and promptly by X-ray reprocessing in the outer accretion disk or in the X-ray-heated face of the secondary (van Paradijs & McClintock 1995). While both of these effects do occur in LMC X-3, the extra complicating factor for this source is the variable mass accretion rate in the outer disk that produces an additional, large-amplitude component of optical and (delayed) X-ray variability (Brocksopp et al. 2001; Steiner et al. 2013).

The absorbing column depth to LMC X-3 is

[†]Based on observations made with the Magellan 6.5m Clay telescope at Las Campanas Observatory of the Carnegie Institution and on data products from observations made with ESO Telescopes at the Paranal Observatory under programme ID 074.D-0143

stable and extraordinarily small, $N_{\text{H}} = 3.8_{-0.7}^{+0.8} \times 10^{20} \text{ cm}^{-2}$ (Page et al. 2003) and, correspondingly, the optical extinction is low, $A_{\text{V}} \approx 0.2$ mag. Also, the X-ray spectrum is normally disk-dominated (Wilms et al. 2001; Steiner et al. 2010). This combination of low absorption and a soft spectrum, combined with the persistence of the source, has made LMC X-3 a touchstone for testing accretion disk models (Davis et al. 2006; Kubota et al. 2010; Straub et al. 2011), and for stringently testing the stability of the inner disk radius as a foundation for the measurement of black hole spin (Steiner et al. 2010).

Davis et al. (2006) have used the continuum-fitting method to estimate the dimensionless spin parameter of the black hole primary in LMC X-3 to be $a_* \lesssim 0.3$, a value that depends strongly on the provisional estimates of the black hole mass M and inclination i that are discussed above (Cowley et al. 1983; Kuiper et al. 1988). In this paper, which is based on an extensive collection of spectroscopic and photometric data, we present a new dynamical model for LMC X-3. In a companion paper (Steiner et al. 2014), we make use of the precise values of M and i reported herein, the secure distance to LMC X-3, and extensive archival X-ray data (Steiner et al. 2010) to obtain a firm estimate of the black hole’s spin.

This paper is organized as follows. We discuss the new and archival spectroscopic observations in §2 and the new and archival photometric observations in §3. In §4 we discuss the analysis of the spectra including the measurement of the radial velocities, the rotational velocity, and the detection of emission lines in some of the spectra. In §5 we first present our extensive collection of light curve data, and we then present our dynamical model. We discuss several topics and offer our conclusions in §6.

2. Observations

2.1. Magellan Spectroscopic Observations

Our echelle spectra obtained using the Magellan Inamori Kyocera Echelle (MIKE) spectrograph (Bernstein et al. 2002) and the 6.5 m Magellan Clay telescope at Las Campanas Observatory (LCO) were previously discussed in Song et al. (2010), but for completeness many of the details are given here. Fifty-four spectra of the op-

tical counterpart of LMC X-3 (Warren & Penfold 1975) along with the spectra of several flux standards and spectral-comparison stars were obtained on the nights of 2005 January 20–24, 2007 December 20–21, and 2008 February 27 through 2008 March 1. MIKE was used in the standard dual-beam mode with a $1''.0 \times 5''.0$ slit and the 2×2 binning mode. The $1''$ slit width was well-matched to the seeing, which was between $0''.7$ and $0''.9$ for the 2005 run, $0''.8$ to $1''.2$ for the 2007 run, and $0''.6$ and $1''.2$ for the 2008 run. The wavelength calibration was provided by exposures of a ThAr lamp, obtained before and after each pair of observations of the object. We used data from the blue arm, which has a wavelength coverage of 3430–5140 Å and resolving power of $R = 33,000$.

The results presented in Song et al. (2010) were based on reductions of the MIKE spectra carried out with an IDL-based pipeline written by Scott Burles¹. Since that time we have found a possible problem with the heliocentric wavelength corrections. Also, the order merging was less than ideal. We therefore carried out a new and independent reduction using a pipeline written by Dan Kelson². As part of these reductions, the blaze function was mostly removed by dividing the spectra by the fitting functions used to normalize the flat-field exposures. To merge the echelle orders, the spectrum in each order was normalized using cubic splines and the low signal-to-noise ends were cut so that there was 5 to 10 Å of overlap between adjacent orders. The signal-to-noise ratio per pixel near the peaks of the blaze function was generally in the range of $\approx 20 - 40$ for most of the spectra.

2.2. UVES Spectroscopic Observations

We also made use of five spectra obtained with the UVES instrument on the second 8.2m telescope at the European Southern Observatory, Paranal. The observations were taken in service mode between 2004 December 19 and 2005 March 20. The integration times were 2120 seconds each with seeing conditions between 0.8 and 2.2 arcseconds. A slit width of 2 arcseconds was used in combination with the dichroic #2 yielding a resolving power of $R = 20,000$ and a useful wave-

length coverage of 3756 Å to 4975 Å. The setup procedure for the instrument ensures the star is precisely centered on the slit, even when the seeing is less than the slit width used. The spectra were fully reprocessed, calibrated, and merged by the ESO UVES pipeline³. The typical signal-to-noise ratios per pixel were around 30 at a wavelength of 4250 Å. Results based on these data have been published by Val Baker et al. (2005).

3. Photometric Observations

3.1. SMARTS Observations

LMC X-3 was observed using the ANDICAM instrument on the SMARTS 1.3m telescope at Cerro Tololo between 2007 October 5 and 2011 January 25. The source was observed on most nights when it was available at an airmass of less than ≈ 1.6 . An observing sequence consisted of observations in the *B*, *V*, *I*, and *J* filters, with exposure times of 180 seconds each in the optical filters and 30 seconds in each of 15 dithered images in *J*. The data were processed using the SMARTS pipeline in IRAF. Differential light curves were obtained using two nearby stars in *B*, 4 stars in *V*, 6 stars in *I*, and 6 stars in *J*. The observations were placed on the standard scales using observation of stars from Landolt (1992) for the optical and stars from Persson et al. (1998) for *J*. In all, observations of standards from 45 nights in *B*, 44 nights in *V*, 46 nights in *I*, and 76 nights in *J* were used to establish the zero-points.

3.2. Archival Data

There have been previous studies of LMC X-3 in the optical, and we have made use of published data from two sources. Brocksopp et al. (2001) carried out one of the larger studies, where they obtained optical observations over a period spanning 6 years. Specifically, observations in *B* and *V* were made between 1993 and 1999 during 16 separate observing runs, each of one to four weeks in duration. The calibrated light curves were kindly sent to us by C. Brocksopp. Our second source of archival optical data is van der Klis et al. (1985) who obtained *B* and *V*-band CCD photometry of LMC X-3 from 1983 November 15–20. The times

¹<http://web.mit.edu/~burles/www/MIKE/>

²<http://code.obs.carnegiescience.edu/carnegie-python-distribution>

³version 3.2, see <http://www.eso.org/observing/dfo/quality/reproUVES/processing.html>

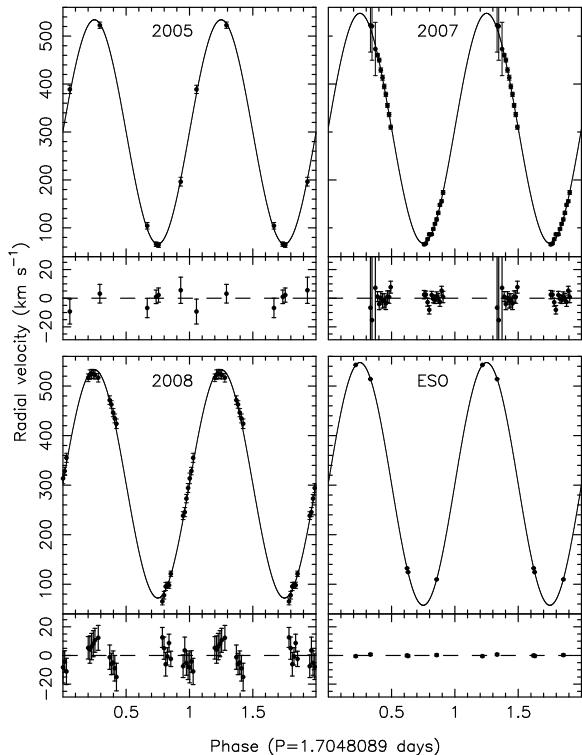


Fig. 1.— The phased radial velocities of LMC X-3 from the different observing runs are shown with the best-fitting models. Two cycles are shown for clarity. See Table 1 for the model parameters.

and differential B and V magnitudes were taken from their Table 1.

4. Spectroscopic Analysis

Many of the quantities needed for the dynamical model discussed below can be measured from the spectra. We used the software tools SYNSPEC (version 49) and SYNLOT (version 2.1) written by Ivan Hubeny (Hubeny, Stefl, & Harmanec 1985; Hubeny 1998) to generate model spectra interpolated from the BSTAR2006 grid (Lanz & Hubeny 2007) to provide templates for the radial velocity extraction and to determine the values of the effective temperature, gravity, and rotational velocity of the companion star. We discuss below our improved radial velocity curves and revised ephemeris, and the spectroscopic parameters of the companion star.

4.1. Radial Velocities Measurements

An improved ephemeris derived from the MIKE spectra and the spectra of Cowley et al. (1983) was given in Song et al. (2010), and the reader is referred to that publication for the full details. The radial velocities we derived from the re-reduced spectra confirm this ephemeris.

An improved cross-correlation analysis (Tonry & Davis 1979) was used to derive radial velocities from all of the MIKE spectra and the UVES spectra. For the template we used a synthetic spectrum with the same resolving power, wavelength sampling, and rotational velocity as the object spectra. The wavelength region used in the analysis was 4000 – 4060 Å, 4158 – 4290 Å, 4376 – 4790 Å, and 4910 – 5000 Å, which excludes the broad Balmer lines. Our previous ephemeris was found by using the MIKE radial velocities along with the radial velocities from Cowley et al. (1983). To account for possible differences in the zero-points of the velocity scales, a circular orbit model was fitted to each data set and the respective systemic velocities were removed. We repeated this exercise by using our new MIKE radial velocities, the UVES radial velocities, and the Cowley et al. radial velocities and found essentially the same ephemeris that was reported in Song et al. (2010). We therefore adopt that ephemeris in the analysis reported below.

LMC X-3 is highly variable in X-rays. Given the X-ray variability, the radial velocity measurements were divided up into four sets: the measurements from the UVES spectra and the measurements from the 2005, 2007, and 2008 MIKE spectra. In Table 1 we give average 2–12 keV X-ray intensities from the *RXTE* All Sky Monitor (ASM). Since the ASM did not continuously observe a given source, some interpolation is needed. We used a smoothing and interpolation scheme based on both the ASM and PCA data to estimate the source brightness. The error bars given in the table come from a Monte-Carlo code that varied the intensities using the nominal ASM and PCA error bars. While not ideal, we believe this is a reasonable way to gauge the instantaneous X-ray intensity and its uncertainty. Each 2–12 keV intensity value was then converted to a bolometric X-ray luminosity using the procedure outlined in Appendix A. Finally, a three parameter sinu-

TABLE 1
SPECTROSCOPIC PARAMETERS OF LMC X-3

parameter	MIKE 2005	MIKE 2007	MIKE 2008	ESO UVES
period (days)	1.7048089 ^a	1.7048089 ^a	1.7048089 ^a	1.7048089 ^a
T_0 (HJD 2,450,000+)	3391.1914 ± 0.0069	4454.9963 ± 0.0024	4523.1196 ± 0.0032	3449.1600 ± 0.0007
K_2 (km s ⁻¹)	233.97 ± 3.46	239.85 ± 2.19	230.52 ± 2.91	245.01 ± 0.42
γ (km s ⁻¹)	300.08 ± 3.14	307.72 ± 1.29	302.62 ± 1.81	303.43 ± 0.35
rms (km s ⁻¹)	5.472	4.822	7.787	0.434
N	6	24	24	5
ASM intensity (counts s ⁻¹) ^b	1.99, 0.05	0.86, 0.01	2.22, 0.02	2.37, 0.63
$\log(L_x/\text{erg s}^{-1})$ ^c	38.25 ± 0.13	37.88 ± 0.42	38.29 ± 0.08	38.32 ± 0.18
ΔK (km s ⁻¹)	3.97 ± 0.74	2.26 ± 0.81	4.28 ± 0.51	4.47 ± 0.86
K_{corr} (km s ⁻¹)	237.9 ± 3.5	242.1 ± 2.3	234.8 ± 3.0	249.5 ± 1.0

^aFixed.

^bX-ray intensity from the *RXTE* All Sky Monitor. The quoted numbers are the average count rate and the standard deviation of the individual measurements given in Table 2.

^c L_x (erg s⁻¹) = (ASM rate) × (8.85 × 10³⁷). The uncertainty includes the uncertainty on the individual ASM measurements.

soid was fitted to each data set with the period fixed at $P = 1.7048089$ days (the formal uncertainty on the period is 0.0000011 days, Song et al. 2010), yielding the parameters given in Table 1. The phased data and best fitting models are shown in Figure 1.

We find some scatter in the resulting K -velocities with a low value of $K_2 = 230.52 \pm 2.91$ km s⁻¹ for the 2008 MIKE spectra to a high value of 245.01 ± 0.42 km s⁻¹ for the UVES spectra. For comparison, Cowley et al. (1983) found $K_2 = 235 \pm 11$ km s⁻¹, and Val Baker et al. (2007) found $K_2 = 242.4 \pm 4.3$ km s⁻¹ from the UVES data (this is their measurement before they applied a correction for X-ray heating). Also, the quality of the fits (judging by the rms of the residuals) varies, ranging from 0.434 km s⁻¹ for the five ESO measurements to 7.787 km s⁻¹ for the 24 MIKE measurements from 2008. For the three MIKE data sets, there is a weak inverse correlation between the K -velocity and the X-ray luminosity L_x , which is discussed in §5.2.

4.2. Emission Lines

Generally speaking, the optical spectra of LMC X-3 are dominated by the absorption line component due to the secondary star. However, during the first three MIKE observations from the night

of 2007 December 21 at an orbital phase of 0.34, an emission feature was seen in the blue wings of the Balmer lines (Figure 2). A simple differencing process using the first five observations from that night was used to isolate the emission components in the Balmer lines. We used the spectra directly from the reduction pipeline (counts vs. wavelength for individual orders) with the blaze function mostly removed. The orders that contain H β , H γ , and H δ were each normalized to approximately unity by dividing by their respective mean count rate. The fifth spectrum was subtracted from each of the first four spectra (the fourth spectrum has no emission lines and serves as a “control” spectrum), and unity was added to the difference spectra to put the continuum at 1.0. The results are shown in Figure 3. The difference spectra from the first three observations show emission lines that are reasonably well modeled by Gaussians with full widths at half maximum of ≈ 600 km s⁻¹ and equivalent widths between 3 and 4 Å. The emission appears to be gone by the fourth observation. The He I lines show a hint of a blue-shifted emission, albeit at a much smaller level than in the Balmer lines. The radial velocities derived using these three spectra (derived using the He I and other metal lines) show more scatter than the other measurements from 2007, but they are still within about 20 km s⁻¹ of

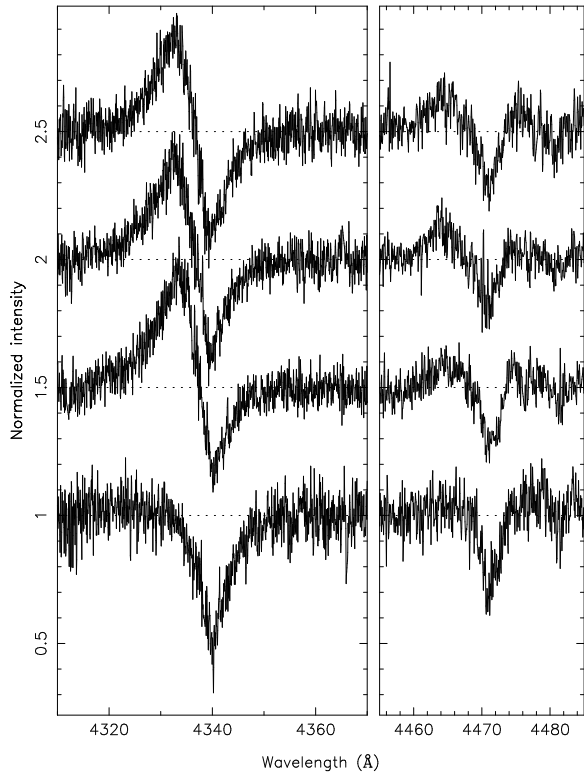


Fig. 2.— Normalized spectra near $H\gamma$ (left) and He I (right) for the first four MIKE observations from 2007 December 21, with the earliest observation shown at the top. The orbital phases are 0.333, 0.346, 0.372, and 0.389. A clear emission component is seen in $H\gamma$ and other Balmer lines. While the signal-to-noise ratios are relatively poor, this emission feature is relatively weak or absent in the He lines.

the model curve (Figure 1). The uncertainties on these three points were inflated by a factor of 10 so that they would receive very little weight in the sinusoid fit.

The emission features in the Balmer lines were observed in $\approx 6\%$ of the MIKE spectra, and in none of the UVES spectra. Cowley et al. (1983) noted the “occasional, very weak P Cygni emission at $H\beta$ ”, but did not specify the number of spectra that contained this feature. The origin of these emission lines is not immediately clear. The radial velocities of the emission lines from the first three observations are roughly consistent with the expected radial velocity of the black hole, which may suggest an origin in the accretion disk. However,

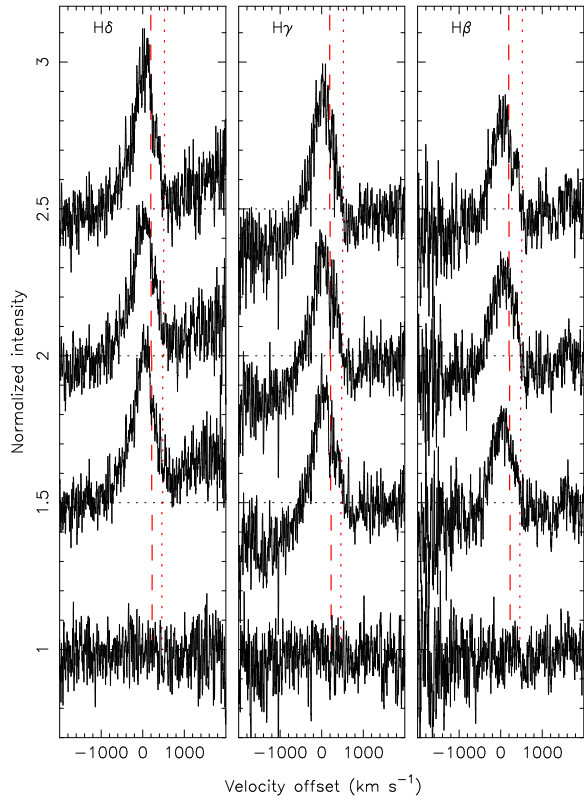


Fig. 3.— This figure shows the differences between the first four spectra from the night of 2007 December 21 relative to the fifth spectrum from that night, in velocity units near $H\beta$, $H\gamma$, and $H\delta$. The orbital phases are 0.333, 0.346, 0.372, and 0.389. The vertical dotted lines denote the radial velocity of the secondary star, and the vertical dashed lines denote the approximate radial velocity of the black hole. The residual Balmer emission lines are evident in the first three observations. The features are reasonably well fit by Gaussians with FWHMs near 600 km s^{-1} , centroid velocities between 0 and 50 km s^{-1} (for reference the systemic velocity is 300 km s^{-1}), and equivalent widths between 3 and 4 \AA . The emission lines appear to be completely gone by the fourth observation.

if this is the case, the emitting region probably did not cover the entire disk because the profiles are not double-peaked. The rapid disappearance of the emission may suggest an association with a rapidly varying region such as the mass transfer stream. However, if this is the case, the radial velocity of the emitting gas should more closely

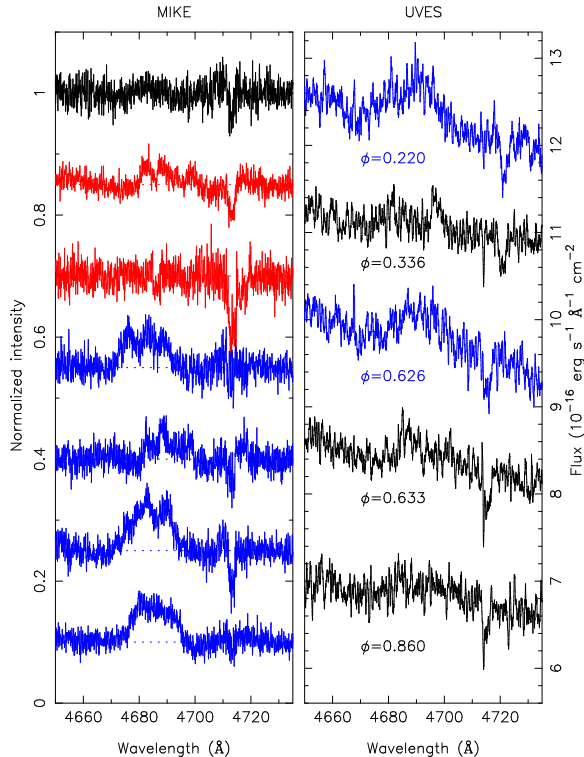


Fig. 4.— Left: Normalized “restframe” spectra of the MIKE observations near the He II $\lambda 4686$ line, averaged from each night or run. From top to bottom, the spectra are from 2005 (6 nights), night 1 of 2007 (12 spectra), night 2 of 2007 (9 spectra), night 1 of 2008 (6 spectra), night 2 of 2008 (6 spectra), night 3 of 2008 (5 spectra), and night 4 of 2008 (7 spectra). No emission feature is seen in the 2005 observations or in the spectrum from the second night of 2007. A broad emission line is present in all of the spectra from 2008, especially from the last two nights. The absorption line near 4713 \AA is He I. Right: The five UVES observations are shown smoothed with 15 point running means. The vertical scale is in flux units, and vertical offsets have been applied for clarity. The spectra are ordered by orbital phase, and no Doppler correction has been applied. The two spectra at orbital phases 0.220 and 0.626 (shown in blue) appear to have the strongest He II emission line.

match the radial velocity of the secondary star (e.g. Gies & Bolton 1986).

In addition to the Balmer emission, there is, on occasion, a broad emission feature which is al-

most certainly due to He II $\lambda 4686$ (see Figure 4). This feature, which is commonly seen in actively accreting X-ray binaries, seems to be strongest in the 2008 MIKE observations, and is either very weak or absent in the 2005 and 2007 MIKE observations. Perhaps not surprisingly, the mean X-ray intensity was higher for the 2008 observations than it was for the 2005 and 2007 observations. Owing to the large width (about 15 \AA), properly normalizing the spectra to the local continuum is a challenge. The MIKE spectra are not flux calibrated so we cannot measure the emission line flux. Typical values for the equivalent widths of the He II feature seen in 2008 range from about 0.8 to 1.2 \AA .

The He II emission line is detectable in two of the five UVES spectra (Figure 4 shows the UVES spectra smoothed with a 15 point running mean). The line flux is on the order of $1.2 \times 10^{-16} \text{ erg s}^{-1} \text{ cm}^{-2} \text{ \AA}^{-1}$, and the equivalent width is about 1.4 \AA . The two spectra where the line is detected were taken 2005 March 19 and 20 (at orbital phases 0.626 and 0.220). The X-ray luminosity was about a factor of 1.5 times larger than it was during the three previous UVES observations. Although the signal-to-noise ratios are not large, it does appear that the He II emission line is moving out of phase relative to the nearby He I absorption line. This suggests that the He II emission is coming from the accretion disk and not the heated part of the secondary star.

4.3. Stellar Parameters and the Rotational Velocity

As noted above, LMC X-3 is extremely variable in the optical, where excursions of up to $\approx 1 \text{ mag}$ have been observed (Brocksopp et al. 2001). Some B-stars are known to be pulsational variables (e.g. stars of the β Cephei type) with typical periods less than about one day. Both the light and radial velocity curves can be affected by these pulsations. Since many of the light curves of LMC X-3 look cleanly ellipsoidal and since the well-sampled radial velocity curves are smoothly sinusoidal, we will assume that (apart from ellipsoidal variability) the B-star in LMC X-3 is intrinsically non-variable. Given this, the large excursions in the mean brightness level are most likely due to a variable component of disk light, which implies that the spectra contain at least a small contribution of light from the accretion disk. We therefore used

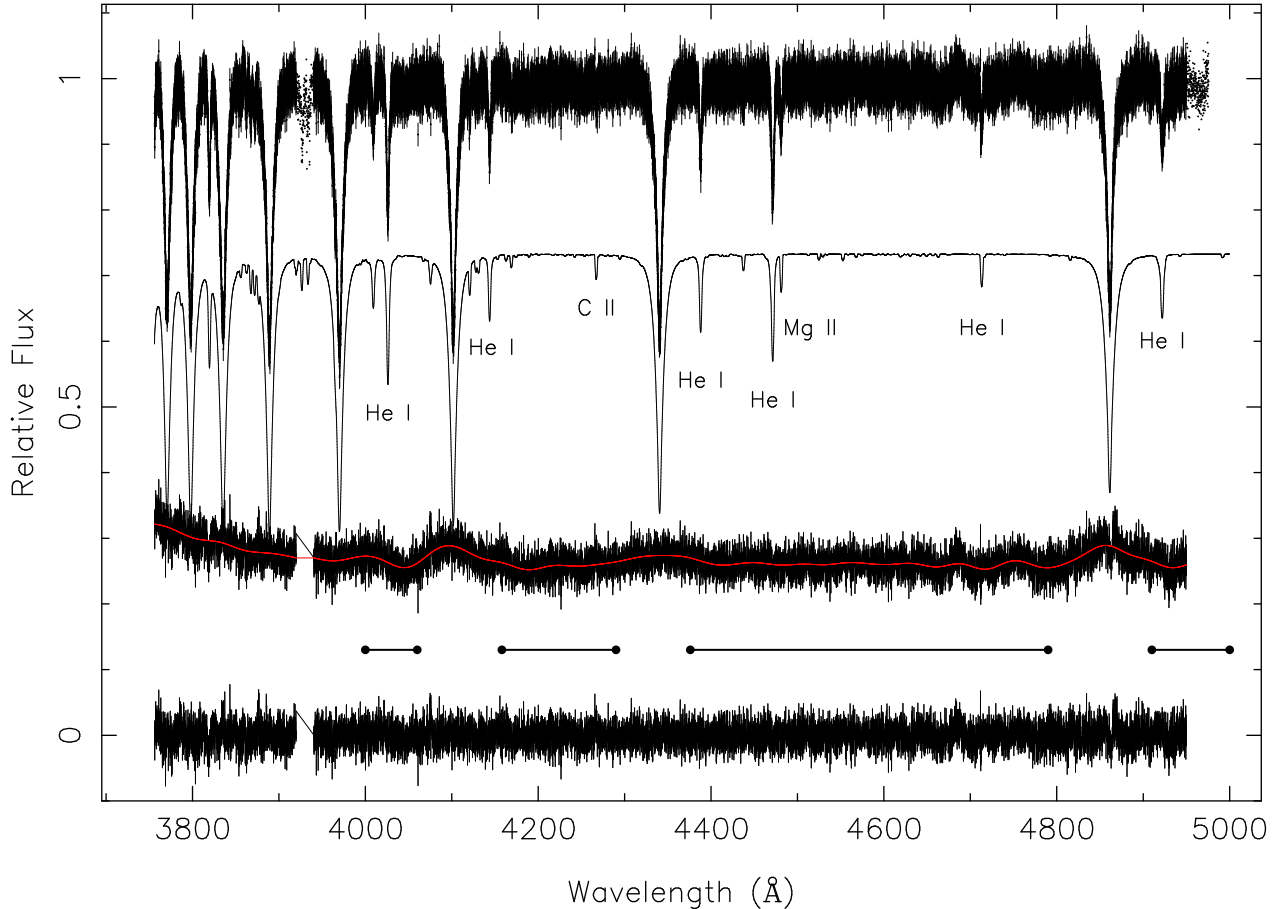


Fig. 5.— An illustration of the process used to model the spectra is shown. The spectra are, from top to bottom, the normalized restframe spectrum made from the UVES spectra; a normalized model spectrum with $T_{\text{eff}} = 16,435$, $\log g = 3.801$, and $V_{\text{rot}} \sin i = 121.4 \text{ km s}^{-1}$, scaled by 0.76; the difference between the restframe spectrum and the scaled model; and the difference between the residuals and a smoothed version of itself. The stellar features are removed in the final spectrum. In this case, the star contributes 76% of the light in this wavelength region.

the method outlined in Marsh, Robinson, & Wood (1994) to decompose the spectra into the stellar absorption line component and the accretion disk component. Briefly, the spectrum to be fitted is normalized to its continuum. A model spectrum is constructed from the BSTAR2006 models (using the LMC metallicity grid) with a given temperature T_{eff} , gravity $\log g$, and rotational velocity $V_{\text{rot}} \sin i$. The model is scaled by a weight k (where k is the fraction of the total light that is contributed by the star) and subtracted from the observed spectrum. A heavily smoothed version of the difference spectrum is subtracted from the difference spectrum itself, and the χ^2 of the resid-

uals is computed. The value of k is varied until the value of χ^2 is minimized. Spectra at various stages of this process are shown in Figure 5.

For the purposes of determining the rotational velocity (which is needed for the dynamical model), the UVES spectra are superior to the MIKE spectra owing to their better signal-to-noise, flux calibration, and order merging. We tried three ways of fitting the spectra to derive a rotational velocity: (i) using all H, He, and metallic lines in the (Doppler-corrected) averaged UVES spectrum; (ii) using all H, He, and metallic lines in each UVES Doppler-corrected spectrum and

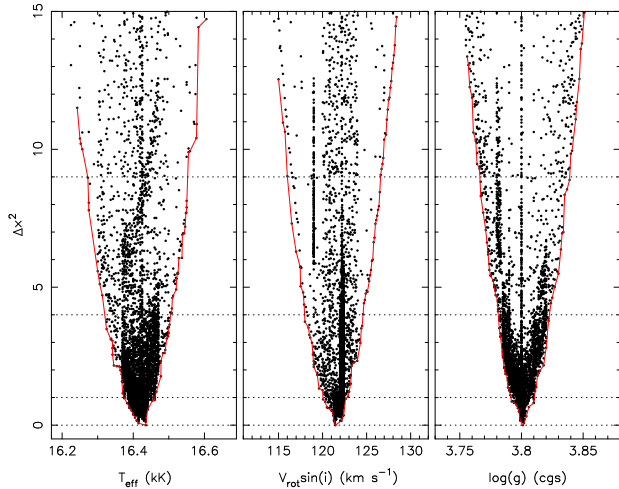


Fig. 6.— Plots of χ^2 vs. the effective temperature (left), the rotational velocity (middle), and the gravity (right) are shown from the fit of the average UVES restframe spectrum. The horizontal dotted lines denote the 1σ , 2σ , and 3σ confidence regions.

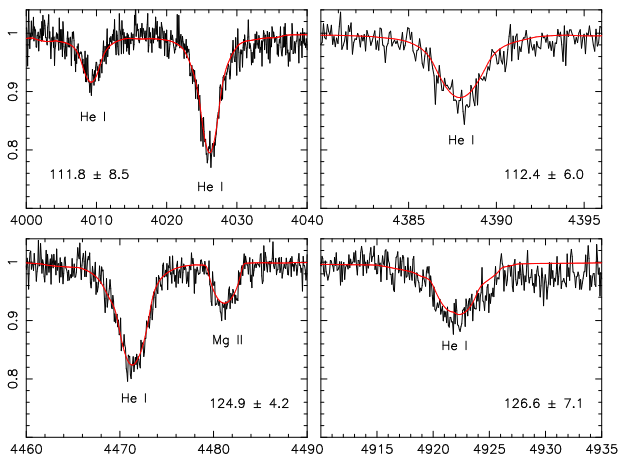


Fig. 7.— Model fits to individual lines (or close pairs) in the restframe UVES spectrum. The derived rotational velocity is shown in each panel.

averaging the individual measurements; and (iii) using individual strong He and metallic lines in the average UVES spectrum. The fourth possible way, namely using individual strong He and metallic lines in each spectrum did not add any useful information owing to the relatively low signal-to-noise. For each case, the decomposition technique was applied using template spectra drawn from

a dense model grid with a wide range of temperatures, gravities, and rotational velocities. The χ^2 values for each template were recorded, and marginalized distributions of χ^2 over each parameter of interest were generated (see Figure 6 for the distributions from the fit to the average UVES spectrum). The parameter values are summarized in Table 2. The rotational velocity derived from the average spectrum (e.g. case (i) above) is $V_{\text{rot}} \sin i = 121.4 \pm 1.4 \text{ km s}^{-1}$. For case (ii), the average of the rotational velocities derived from the individual spectra is $V_{\text{rot}} \sin i = 118.5 \pm 6.6 \text{ km s}^{-1}$, where the stated uncertainty is the formal error in the mean. Model fits to individual (or close pairs) of He I lines in the average UVES spectrum (case (iii) above) are shown in Figure 7. The average of the four measurements is $118.9 \pm 3.6 \text{ km s}^{-1}$.

The rotational velocities derived for the three cases above are all in good agreement. We note that the X-ray luminosity during the first three UVES observations was $\approx 60\%$ lower than it was for the last two observations (see Table 2.) Given that averaging spectra with different X-ray luminosities (as in cases (i) and (iii)) may introduce small systematic uncertainties, we adopt the results for case (ii), namely $V_{\text{rot}} \sin i = 118.5 \pm 6.6 \text{ km s}^{-1}$.

For comparison, we also fitted the 51 individual MIKE spectra that did not have emission lines and the restframe spectra made from nightly averages (in the case of the 2005 run all six spectra were combined into a restframe spectrum). The results are given in Table 2. The average of the 51 measurements is $127.2 \pm 3.5 \text{ km s}^{-1}$ and the median value is 118.2 km s^{-1} , both of which agrees well with the rotational velocity derived from the UVES spectra that we adopt above.

As a consistency check, we point out that owing to the peculiarities of Roche geometry, the mean density of a Roche-lobe filling star mainly depends on the orbital period of the binary. For a fixed orbital period, there is little variation in the stellar density over a wide range of mass ratios (e.g., Eggleton 1983). In that same vein, the surface gravity of the companion is weakly dependent on the mass ratio of the binary and is usually well determined from the light curve models. In the model discussed below, we find $\log g = 3.73$ for the secondary star. This dynamical measure-

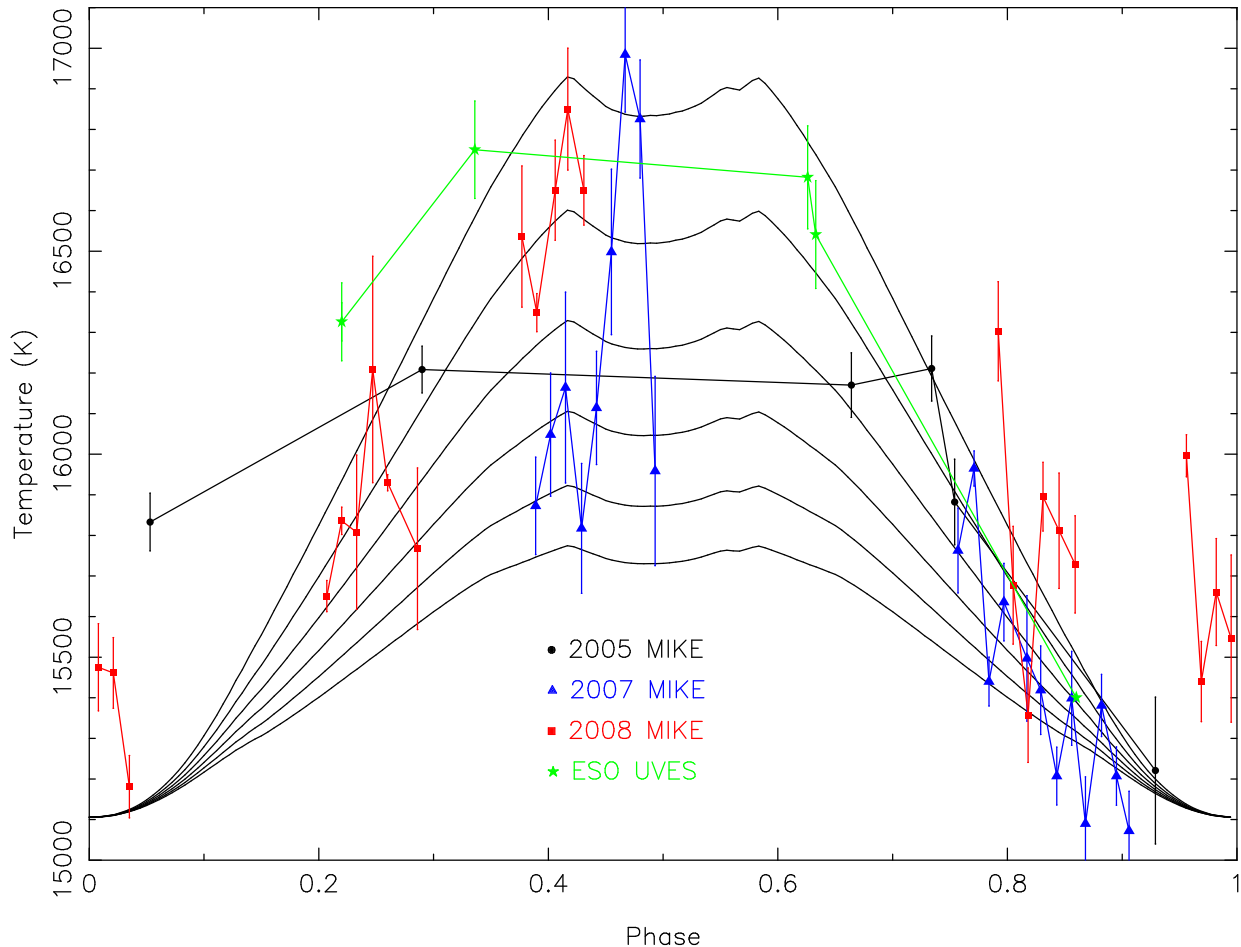


Fig. 8.— The effective temperatures derived from the individual spectra are shown as a function of the orbital phase. Measurements from the same night or run (in the case of the 2005 MIKE spectra and the ESO UVES spectra) are connected by lines. The solid curves are models with an intrinsic stellar temperature of 15,100 K (chosen to illustrate the effect), and $\log(L_x/\text{erg s}^{-1}) = 38.0$ (lower-most curve) to $\log(L_x/\text{erg s}^{-1}) = 38.5$ in equal intervals.

ment of the gravity is in good agreement with the spectroscopically-determined values: All of the gravities measured from the individual UVES spectra are within 0.12 dex of the dynamical measurement, and the gravity found from the mean UVES spectrum is within 0.05 dex. The gravities from the individual MIKE spectra show considerably more scatter, where the mean gravity is $\log g = 3.45$ and the standard deviation is 0.27 dex.

We note that the temperatures measured for the individual spectra vary with orbital phase, as shown in Figure 8. Observations taken near phase

0 (inferior conjunction of the companion star) tend to have smaller effective temperatures whereas observations taken near phase 0.5 (when the companion star is farthest from the observer) tend to have higher temperatures. The change in the observed temperature with orbital phase is almost certainly due to X-ray heating. Near phase 0, the heated part of the star is mostly directed away from the observer, so the parts of the star that are visible are cooler. On the other hand, the heated face of the star is most visible near phase 0.5, and as a result the observed temperature near that phase tends to be higher. Using the ellipsoidal model discussed below, we computed the intensity-weighted

TABLE 3
PHOTOMETRIC DATA FOR LMC X-3

#	Data subset label	JD range (-2,440,000)	UT range (YYYY/MM/DD)	Number of V-band	Number of B-band	Reference ^a
1	A93	9266.86-9275.87	1993/10/06-1993/10/15	72	6	1
2	W94	9705.62-9726.58	1994/12/19-1995/01/09	24	23	1
3	W95	10059.55-10069.83	1995/12/08-1995/12/18	54	52	1
4	S96	10148.59-10156.59	1996/03/06-1996/03/14	12	11	1
5	A96a	10324.84-10340.90	1996/08/29-1996/09/14	63	45	1
6	A96b	10343.78-10353.89	1996/09/17-1996/09/27	42	44	1
7	W96a	10413.58-10423.86	1996/11/26-1996/12/06	38	25	1
8	W96b	10424.70-10441.86	1996/12/07-1996/12/24	47	39	1
9	S98	10856.72-10884.51	1998/02/12-1998/03/12	95	42	1
10	W98	11123.71-11142.86	1998/11/06-1998/11/25	73	26	1
11	vdK	5653.77-5658.81	1983/11/15-1983/11/20	25	10	2
12	Halved	15148.59-15587.68	2009/11/13-2011/01/26	1116	695	3
13	Quartered	14822.72-15553.69	2008/08/13-2010/12/23	74	73	3

^a1: Brocksopp et al. (2001); 2: van der Klis et al. (1985); 3: this work

average temperature of the visible parts of the star as a function of the orbital phase for X-ray luminosities between 10^{38} and $10^{38.5}$ ergs s⁻¹ (which bracket the typical observed values); the results are shown in Figure 8. Although the scatter is large, these models reproduce the changes seen in the temperature with orbital phase. Near phase 0, there is little variation in the observed temperature, regardless of the X-ray luminosity. On the other hand, the observed temperature near phase 0.5 is sensitive to the value of the X-ray luminosity. We cannot expect a perfect match between these simple models and the observations since the observations have large uncertainties and since the X-ray luminosity can change significantly on short time scales. Based on the relatively small number of spectra taken near phase 0, we adopt a range of $15,000 \leq T_{\text{eff}} \leq 15,500$ K for the effective temperature the secondary would have if it were unheated and spherical.

Finally, one can see in Table 2 some trends in k , the fraction of the total light contributed by the star. During 2007, when the average X-ray intensity was lower, the stellar fractions are usually close to 0.9. During 2008, when the average X-ray intensity was higher, the stellar fractions are closer to 0.7. Thus it seems that the amount of disk light (e.g. the value of $1 - k$) roughly tracks the observed X-ray intensity. Cowley et al. (1983) also found diluted line strengths, noting that “al-

though the *relative* line strengths are normal, all the lines are ~ 2 times too weak compared with a standard B3 main-sequence star...”.

5. Dynamical Models

5.1. Light Curve Selection

LMC X-3 is a highly variable source at both X-ray and optical wavelengths. Thus it is not advisable to simply model all of the photometric data simultaneously. We divided these data into 13 data sets as follows. Brocksopp et al. (2001) had 16 different observing sessions, each lasting about one to four weeks. They labeled these sessions after the season and year, as in S96 for the (Northern Hemisphere) spring of 1996, W98 for the (Northern Hemisphere) winter of 1998, etc. The folded light curves from eight of these sessions had excessive scatter, too few points, or both, and were discarded: A95, A97, A98, S95, S97, S99, W93, and W97. In the case of two extended sessions, A96 and W96, we subdivided each session into a pair of sessions, thereby increasing our sample of clean folded light curves. Thus, the data of Brocksopp et al. (2001) yielded 10 sets of light curves: A93, A96a, A96b, S96, S98, W94, W95, W96a, W96b, and W98.

The B and V light curves taken from van der Klis et al. (1985) constitute an eleventh data set. There are 25 measurements in V and 10 measure-

ments in B , taken over a span of five nights.

In contrast to the Brocksopp et al. (2001) data, which consisted of targeted observing runs over relatively short timescales, the SMARTS observations consist of usually one set of B , V , I and J observations per night over the span of an entire season. For this sampling, the long-term aperiodic variability of the source is a significant problem in modeling the ellipsoidal light curves. We filter out much of the variability by using the *RXTE* All-Sky Monitor (ASM) X-ray light curve, which we interpolate after smoothing it using a Gaussian kernel with a width of one week. As a minor point, we reject OIR data that deviate by more than 2.5σ from the local mean, where σ is the local rms; less than 1% of the optical data and $\sim 2.5\%$ of the J -band data were rejected. In total, only 17 data points out of 1900 were rejected.

We consider two selections of the SMARTS data. For the first of these, which we refer to as “X-quartered,” we use the smoothed X-ray light curve in two ways to filter the OIR data. (1) We select only those OIR data for which the simultaneous X-ray intensity is among the faintest 25% of the ASM data record, when X-ray heating is minimal and the stellar component of light is most dominant. The upper flux limit to this selection corresponds to a threshold ASM count rate of 0.88 counts per second (equivalent to $L \approx 20\%L_{\text{Edd}}$). (2) In Steiner et al. (2013), we demonstrate that the X-ray emission lags the optical emission by ~ 15 days. Therefore, we reject any OIR data for which the X-ray emission 15 days earlier is above the same threshold of 0.88 ASM counts per second. This criterion eliminates data taken during times when the disk is brightest. These two cuts, which serve to substantially reduce the OIR variability induced by accretion, are stringent; only 285/1883 (16%) of the OIR data survive.

We refer to the second set of selected data as “X-halved.” In this case, we select the OIR data for which the simultaneous X-ray intensity is one-half or less the average intensity (which corresponds to an ASM count rate of 1.45 counts per second). However, unlike the X-quartered case, we here employ the model described in Steiner et al. (2013) to compute the OIR emission attributable to X-ray heating and to viscous dissipation in the outer disk. For the selected data, we subtract from the observed OIR fluxes in each band the contri-

butions predicted by the model due to the disk emission and to X-ray reprocessing. Figure 7 (and related text) in Steiner et al. (2013) makes clear the efficacy of this approach to filtering the data. On average, the fluxes in each band are corrected downward by $\sim 10 - 15\%$. The total number of selected data points is 1013 out of 1883 (54%).

Table 3 gives a summary of the photometric data sets used, including the names, the date ranges, and the number of observations in B and V available for each set.

5.2. ELC Model

5.2.1. Basic Setup and Light Curve Fits

We used the ELC code (Orosz & Hauschildt 2000) to construct our dynamical model of LMC X-3. There are two sources of optical light: the secondary star and the accretion disk. We assume the secondary star is in a circular orbit with synchronous rotation, and that it fills its Roche lobe. The models are insensitive to the temperature of the secondary star, and we use $T_{\text{eff}} = 15,500$ K and consequently set the gravity darkening exponent to 0.25. Specific intensities were computed from model atmospheres from the BSTAR2006 grid (Lanz & Hubeny 2007) with the LMC metallicity. The reprocessing of X-ray radiation from near the compact object (hereafter “X-ray heating”) can alter the temperatures of parts of the secondary star. We use a simple model based on Wilson (1990, see also Zhang, Robinson, & Nather 1986) to account for the heating. The overall amount of X-ray heating is controlled by the X-ray luminosity $\log L_x$. Let F_{irr} be the incident flux of X-rays that can be seen from a given point on the secondary star with coordinates (x, y, z) . If the reprocessed light is completely thermalized, then the new temperature of the point on the secondary becomes

$$T_{\text{new}}(x, y, z)^4 = T_{\text{old}}(x, y, z)^4 + \alpha F_{\text{irr}}/\sigma$$

where σ is the Stefan-Boltzmann constant. The normal range of the parameter α is 0.0-1.0: when the $\alpha = 1$ the reprocessed X-ray radiation is immediately reradiated. For our models of LMC X-3, the X-ray emitting area was assumed to have a disk geometry, and we used $\alpha = 1.0$. The basic accretion disk has four parameters, namely its outer radius r_{out} (expressed as a fraction of the

TABLE 4
ELC MODEL PARAMETERS

Parameter	Meaning	Lower bound	Upper bound
i	inclination (deg)	40	80
L_x	X-ray luminosity (erg s^{-1})	36.0	38.5
K_2	K -velocity (km s^{-1})	225	255
Q	mass ratio (M_2/M_1)	1.6	2.4
$\Delta\phi$	phase shift parameter	-0.04	0.04
T_{disk}	temperature at inner disk edge (K)	15,000	50,000
r_{out}	radius of outer accretion disk edge	0.40	0.99
ξ	power-lower exponent on disk temperature profile	-0.80	0.0
β	opening angle of disk rim (deg)	1.0	5.0
s_{spot}	temperature factor for disk spot	0.9	9.8
θ_{spot}	longitude of disk spot (deg)	0.0	360.0
r_{cut}	cut-off radius of disk spot	0.50	0.99
w_{spot}	angular width of disk spot (deg)	1.0	50.0

black hole’s Roche lobe), the opening angle of the outer disk β_{rim} , the temperature at the inner edge T_{disk} , and the power-law exponent on the temperature profile ξ . After some experimentation, it was found that adding a hot spot to the rim of the accretion disk improved the fits by allowing the disk light to be modulated with phase. The 4 parameters needed to specify the spot on the accretion disk are θ_{spot} (its longitude relative to the line connecting the two stars), w_{spot} (its angular width), r_{cut} (its radial extent), and s_{spot} (its temperature factor by which the underlying temperature in a spot region is scaled). Note that the accretion disk can shield parts of the star from the effects of X-ray heating, an effect that is completely accounted for in the model. X-ray heating of the disk itself is accommodated by varying the temperature profile of the disk. To complete the model, the scale of the binary must be specified, and here we used the inclination i , the mass ratio $Q \equiv M_{\text{BH}}/M_2$, and the K -velocity of the secondary star. All of the light curves were phased on the adopted ephemeris, and a phase shift parameter $\Delta\phi$ was included to account for the small uncertainty in the ephemeris.

We have additional observational constraints on the model that are not directly tied to the optical light curves. (1) The absence of an X-ray

eclipse puts an upper limit on the inclination of the binary (this upper limit depends on the mass ratio). This constraint is imposed by giving models that produce an X-ray eclipse a very large χ^2 value. (2) As noted earlier, we have measured the projected rotational velocity of the secondary star $V_{\text{rot}} \sin i$, and this puts a constraint on the mass ratio (e.g. Wade & Horne 1988). For a given set of model parameters, the expected value of the rotational velocity is computed and the χ^2 contribution relative to the observed value is computed and added to the total χ^2 . (3) The measured K -velocity of the secondary star constrains the binary scale, and its contribution to the χ^2 is computed in a similar fashion as the contribution of the rotational velocity. (Note the K -velocity is also used as an input parameter and it is sampled from a uniform distribution by the optimizing codes discussed below.) Finally, (4) the disk fractions measured from the spectra limit the amount of parameter space allowed. Here we use a two part contribution to the χ^2 : $\chi_k^2 = 0$ if the computed value of $1 - k$ for a model is less than 0.15, and $\chi_k^2 = [(k_{\text{mod}} - 0.15)/0.1]^2$ when $1 - k$ is greater than 0.15, where k_{mod} is the model disk fraction. Models with very large disk fractions are disfavored, whereas models with disk fractions near the observed values of ~ 0.1 to 0.3 are given similar

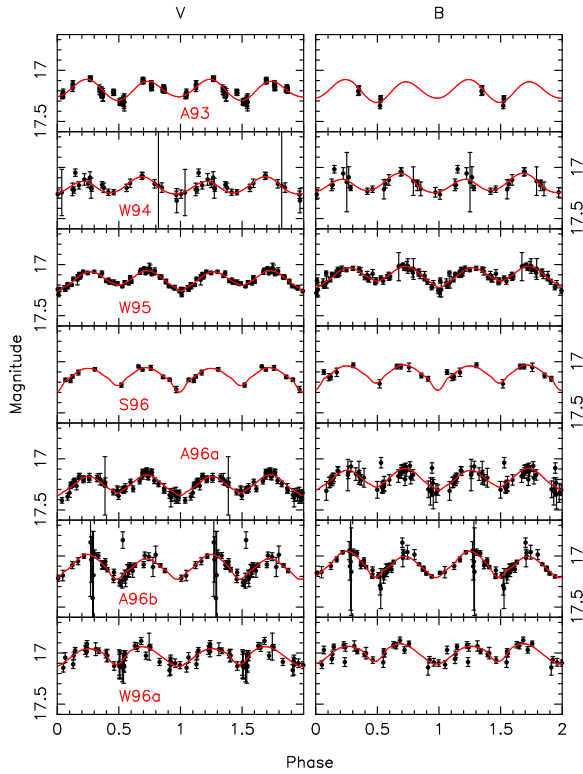


Fig. 9.— The phased V light curves (left panels) and B light curves (right panels) of LMC X-3 for 7 of the 13 observing runs are shown along with the best-fitting models.

weights.

Our model has a total of 13 free parameters, which are summarized in Table 4. The phased light curves were fitted using three of ELC’s optimizers: a Monte Carlo Markov Chain (see Tegmark 2004), a genetic algorithm (Charbonneau 1995), and a Differential Evolution Monte Carlo Markov Chain (Ter Braak 2006). The ranges of each of the free parameters are given in Table 4. After a large number of iterations for each technique, the model giving the smallest χ^2 was identified (Figures 9 and 10). The uncertainties in the fitted and derived parameters were found from the marginalized distributions of χ^2 . The results are given in Tables 5-9, and graphically in Figure 11. As a check, we also fitted the phased light curves assuming no X-ray heating, using only 12 free parameters with the same optimizing schemes. In all of the 13 sets, the derived inclinations are within 11 degrees of each other and range from

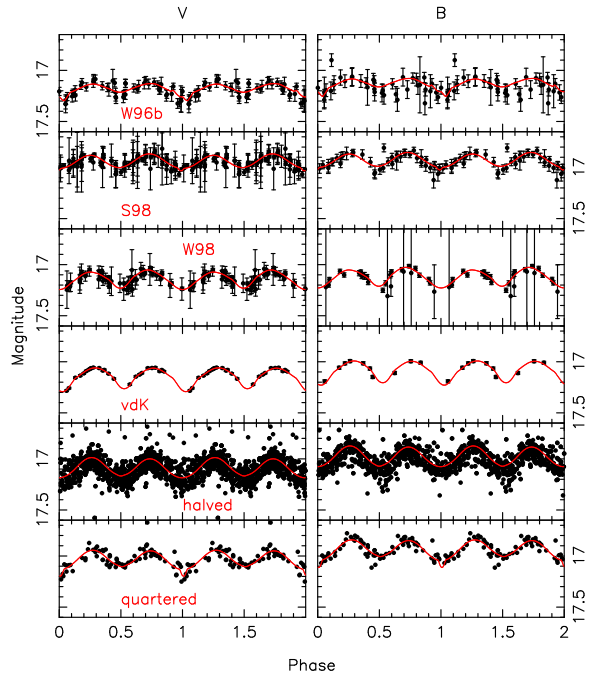


Fig. 10.— The phased V light curves (left panels) and B light curves (right panels) of LMC X-3 for the other 6 observing runs are shown along with the best-fitting models.

62.9° and 72.3° for the models with X-ray heating and from 60.5° and 71.6° for the models without X-ray heating. The other parameters (apart from the B/V disk fractions) are likewise convergent for the 13 data sets. We find that the models with and without X-ray heating generally return very similar parameter values.

Some of the model light curves have a small dip near phase 0.0. The dip is especially noticeable in the quartered light curve, but it is present in other light curves such as W95. This dip is caused by a grazing eclipse of the outer rim of the accretion disk by the secondary star. Given the quality of the light curves, we cannot tell for certain if such a grazing eclipse is real. If it is real, then the inclination would be tightly constrained as there is a very small ranges of inclinations where eclipses of the outer disk occur but eclipses of the X-ray source do not occur.

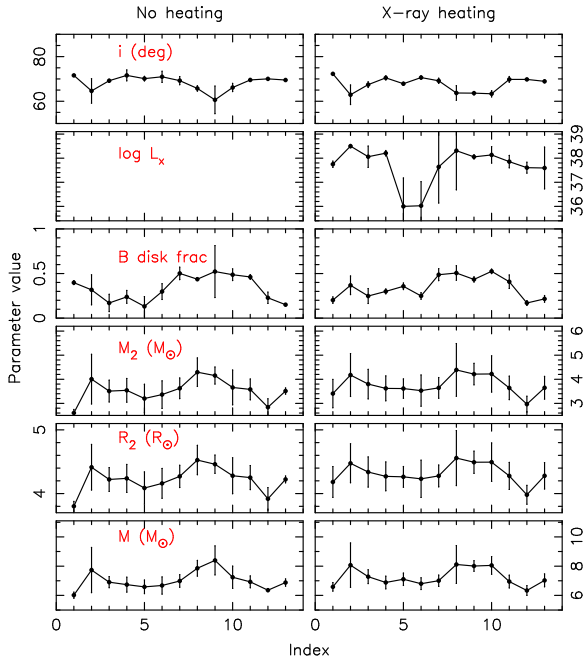


Fig. 11.— The values of selected parameters from the ELC fits plotted as a function of the season (the order of the indices corresponds to the order the light curves are plotted in Figures 9 and 10). The left-hand panels show the models with no X-ray heating, and the right-hand panels show the models with X-ray heating.

5.2.2. K -corrections to the Radial Velocity Curves

In X-ray binaries, the secondary star is not uniformly bright over its surface. Even for an unirradiated star, gravity darkening causes the star to look dimmer near the inner Lagrangian point. If the star is irradiated by the X-ray source, then the hemisphere facing the source appears brighter. In either case, the “center of light” as seen in sky coordinates may not coincide with the star’s center of mass. At a given time, the observed profile of a spectral line is the flux-weighted and Doppler-shifted sum of the individual profiles distributed over the visible portion of the star’s surface. The brightness variations over the surface cause asymmetries in the spectral line profiles, which in turn cause the measured radial velocity to differ from the true radial velocity (Wilson & Sofia 1976). For the simple case of a circular orbit, e.g., this causes the velocity curve to deviate from a sinusoid, and the measured K -velocity to differ from the true K -

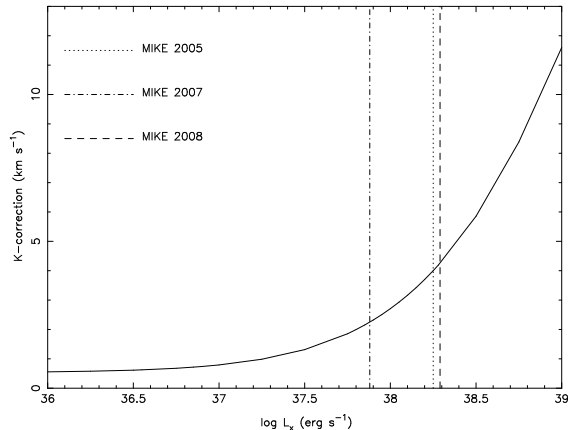


Fig. 12.— The K -correction as a function of the X-ray luminosity. The vertical lines give the X-ray luminosity during each of the three MIKE runs.

velocity. In practice, to obtain the true K -velocity one computes the so-called “ K -correction” and adds it to the observed K -velocity.

The K -correction can be computed in two distinctly different ways. If the X-ray spectrum is “soft”, the X-rays are absorbed near the stellar surface and the absorption lines are “filled in” and are hence considerably weaker than normal (Phillips et al. 1999; Soria et al. 2001). Since in this case the absorption lines one actually observes come mostly from the unheated part of the star, the true K -velocity is *smaller* than the measured one, and the K -correction is *negative*. If, on the other hand, the X-ray spectrum is “hard”, the X-rays are either absorbed below the photosphere or are reflected, which strengthens the absorption lines. In this case, the dominant contribution to the observed absorption lines comes from the heated part of the star and, consequently, the true K -velocity is *larger* than the measured one, and the K -correction is *positive*.

In two ways our data suggest that the K -correction is positive and corresponds to the “hard” case outlined above. First, we observe a change of temperature over the orbit, with the hottest temperatures observed when the inner Lagrangian point is pointed at the observer. If absorption lines were largely absent from that part of the star, then we should not expect to measure such a temperature change. Second, the three MIKE data sets show an anti-correlation between

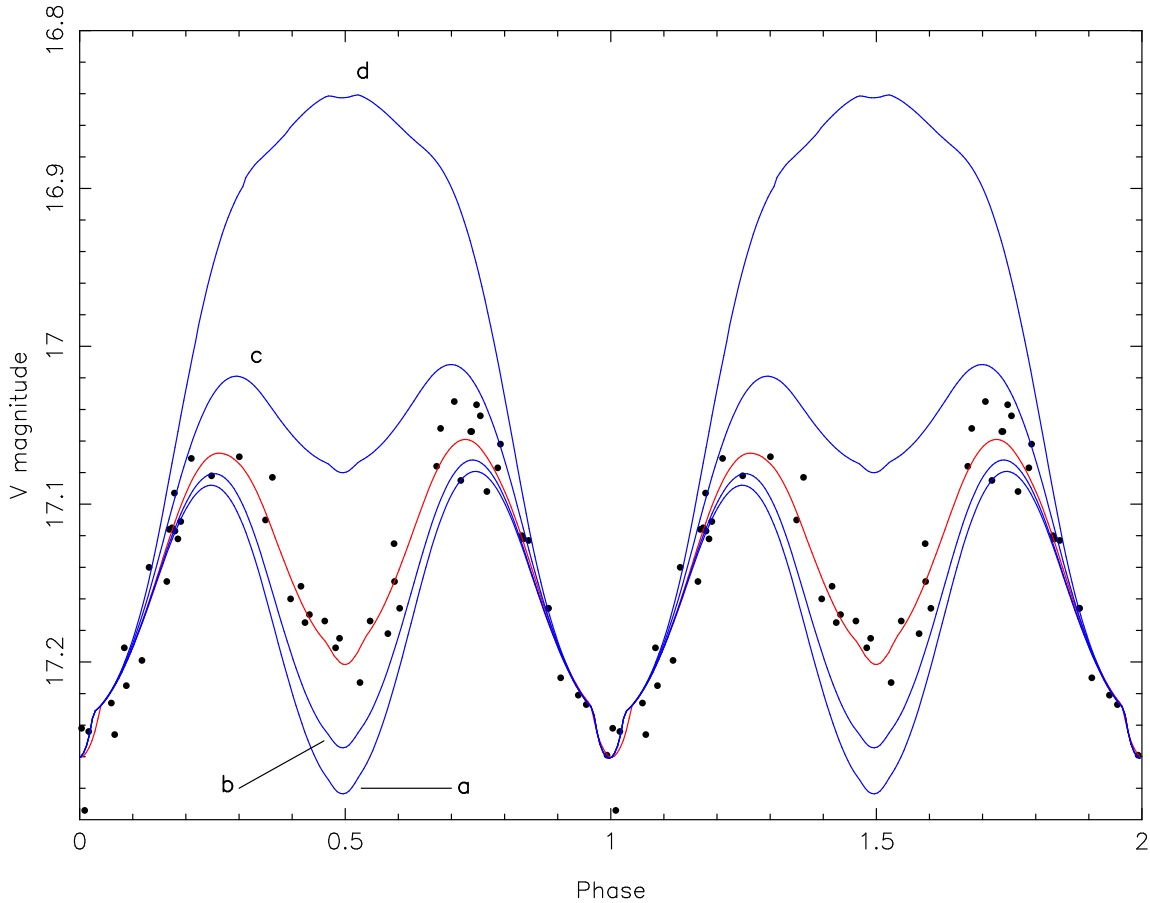


Fig. 13.— The V-band light curve from the W95 data set is shown along with the best-fitting model (red line) with $\log(L_x/\text{ergs}^{-1}) = 38$. This model includes a grazing eclipse of the accretion disk at phase 0; we do not claim that such a feature is definitively present in the data. Four other models with different X-ray heating but otherwise identical parameters are shown in blue. These models are (a) no X-ray heating; (b) $\log(L_x/\text{ergs}^{-1}) = 37.5$ and a disk-like X-ray emitting emitting region; (c) $\log(L_x/\text{ergs}^{-1}) = 38.5$ and a disk-like X-ray emitting emitting region; and (d) $\log(L_x/\text{ergs}^{-1}) = 38.0$ and a point-like X-ray emitting emitting region.

the X-ray luminosity and the K -velocity (Table 1). If one ranks the three MIKE runs in terms of the X-ray luminosity from the lowest to the highest, the ordering is 2007, 2005, and 2008. If one arranges the K -velocities from the largest to the smallest, the ordering is again 2007, 2005, and 2008. The K -velocity from the UVES data does not fit this trend. However, the X-ray luminosity changed significantly between the third and fourth UVES observation. Also, with only five observations the phase coverage is poor.

ELC computes corrections to the model radial velocity curve following the prescription given

in Wilson & Sofia (1976). This corresponds to the “hard” case discussed above, which results in positive K -corrections. To compute the K -corrections, we used the W95 light curve solution as the base model (note that this model includes an accretion disk). The choice of the W95 light curves was somewhat arbitrary, but the results are insensitive to the actual data set used. Light and velocity curves were computed using a wide range of X-ray heating values, and sine curves were fitted to the model curves to measure the model K -velocity. The K -correction is defined as the input K -velocity minus the fitted K -velocity. Figure 12

shows the results. Note that there is still a small K -correction (0.56 km s^{-1}) when the X-ray luminosity is small compared to the bolometric luminosity of the star—this is due to the tidal distortions of the star. The K -correction is about 5 km s^{-1} when $\log(L_x/\text{erg s}^{-1}) = 38.5$, which is at the upper end of the range of the observed X-ray luminosity of the source.

In computing the K -corrections for the four radial-velocity data sets, we estimated the X-ray luminosity using the mean *RXTE* ASM count rates and the standard deviation of the individual ASM measurements (see Table 1 for count rates and luminosities). The count rate was nearly constant for the 2007 and 2008 MIKE runs, somewhat variable for the 2005 MIKE run and highly variable for the UVES run. For a given data set, the standard deviation in the count rate was added in quadrature with the mean uncertainty on an individual measurement to produce the adopted uncertainty on the ASM count rate. Finally, the mean ASM count rate was converted to an X-ray luminosity and the K -correction was computed using the curve shown in Figure 12. The K -corrections and the values of the final corrected K -velocities are given in Table 1.

The typical X-ray luminosity of LMC X-3 ($L_x \gtrsim 5 \times 10^{37} \text{ erg s}^{-1}$) exceeds the bolometric luminosity of the star ($L_{\text{bol}} \sim 4 \times 10^{36} \text{ erg s}^{-1}$) by more than an order of magnitude, so one might expect the effects of X-ray heating to be large. Nevertheless, the K -corrections are modest, with the largest one being $4.47 \pm 0.86 \text{ km s}^{-1}$ for the UVES data. In addition, the light curves are distinctly double-waved, which also points to a modest amount of X-ray heating. In LMC X-3, there are two main reasons why the X-ray heating is weak. First, the geometry of the X-ray emitting area has a disk-like structure rather than a point-like structure. With a disk-like structure, the X-ray source appears to be somewhat foreshortened when viewed from the secondary star. Second, the outer parts of the accretion disk can block the X-rays from hitting parts of the secondary star that are near its equator. The need for a disk-like geometry for the X-ray emitting area is shown in Figure 13, which displays the V -band light curve from W95 and the best-fitting model with $\log(L_x/\text{erg s}^{-1}) = 38$. For comparison we show other models with different X-ray

luminosities but identical parameters otherwise. The X-ray luminosity cannot be much larger than $\sim 10^{38.1} \text{ erg s}^{-1}$ since the depth of the minimum near phase 0.5 becomes too shallow. We also show the model with $\log(L_x/\text{erg s}^{-1}) = 38$ and a point-like geometry. This model can be clearly ruled out by the data since it has a single maximum and a single minimum per orbital cycle.

For our final adopted value of the K -velocity, we begin by taking the average of the four individual measurements given in Table 1. We find $K_2 = 241.1 \pm 2.8 \text{ km s}^{-1}$, where the quoted uncertainty is the error of the mean. To account for possible systematic errors caused by X-ray heating, we add the standard deviation of the four measurements (5.5 km s^{-1}) in quadrature to the formal error in the mean to produce our adopted uncertainty of 6.2 km s^{-1} , thereby giving $K_2 = 241.1 \pm 6.2 \text{ km s}^{-1}$.

5.2.3. Adopted Results

To arrive at our final adopted result, we first find the weighted average of the inclination i from the 13 data sets for both the models with X-ray heating and without. The adopted weights for the individual inclination measurements are taken to be $W = 1/\sigma^2$. Furthermore, when computing the weighted averages, we impose a “floor” on the inclination uncertainty of 0.5° to avoid giving undue weight to those few cases with extremely small uncertainties. As the uncertainty on the adopted inclination, we use the dispersion-adjusted error in the mean. Then, given i and its uncertainty, we compute the mass of the black hole, the mass and radius of the secondary star, and other parameters assuming a K -velocity of $K_2 = 241.1 \pm 6.2 \text{ km s}^{-1}$, an orbital period of $P = 1.7048089$ days, and a rotational velocity of $V_{\text{rot}} \sin i = 118.5 \pm 6.6 \text{ km s}^{-1}$. The computation of the mass ratio Q via $V_{\text{rot}} \sin i / K_2$ involves accurate numerical integrations in Roche geometry. The final quantities are summarized in Table 10 separately for the two models which respectively omit or incorporate treatment of X-ray heating. Given that the models which include X-ray heating are more complete, we adopt the values derived for this case. In particular, we find $M = 6.98 \pm 0.56 M_\odot$.

Figure 14 shows how the uncertainty on the black hole mass depends on the uncertainties of the rotational velocity and the K -velocity. The

TABLE 10
FINAL PARAMETERS OF LMC X-3

parameter	(No heating)	(X-ray heating)
i (deg)	69.84 ± 0.37	69.24 ± 0.727^a
Q	1.93 ± 0.20	1.93 ± 0.20^a
a (R_\odot)	13.08 ± 0.44	13.13 ± 0.45^a
M_2 (M_\odot)	3.58 ± 0.56	3.63 ± 0.57^a
R_2 (R_\odot)	4.23 ± 0.24	4.25 ± 0.24^a
$\log g_2$ (cgs)	3.739 ± 0.020	3.740 ± 0.020^a
M (M_\odot)	6.90 ± 0.55	6.98 ± 0.56^a

^aAdopted value.

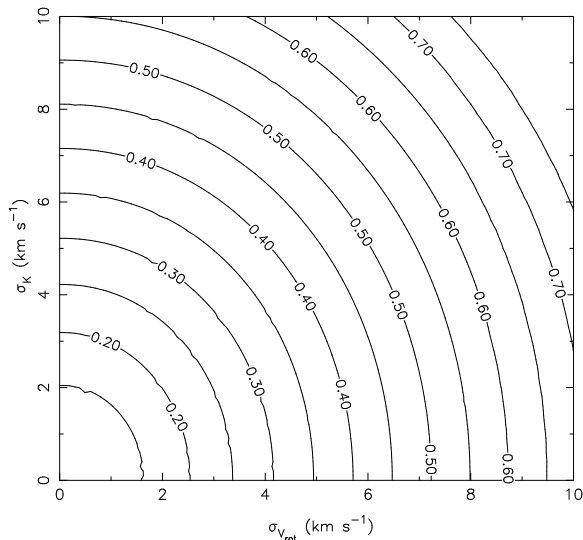


Fig. 14.— The uncertainty on the black hole mass (in M_\odot) as a function of the uncertainty on $V_{\text{rot}} \sin i$ (x -axis) and the uncertainty on the K -velocity (y -axis). The contour levels are spaced every $0.05 M_\odot$, but for clarity only the levels 0.10, 0.20, 0.30, etc. are labeled.

uncertainties in the inclination and the period are included in the computations. When $\sigma_{V_{\text{rot}}} = 6.6 \text{ km s}^{-1}$, the uncertainty in the black hole mass changes modestly for $\sigma_K \lesssim 6 \text{ km s}^{-1}$, since the contour lines are nearly perpendicular to the horizontal axis of the contour plot. Thus most of the improvement in the accuracy of the black hole mass determination must come from an improve-

ment in the determination of the rotational velocity.

5.3. Consistency Check Using the Distance to the LMC

Previously, we have made use of a well-determined distance to the source to put constraints on the dynamical models used to find the black hole mass (and other system parameters) in the high mass X-ray binaries M33 X-7 (Orosz et al. 2007), LMC X-1 (Orosz et al. 2009), and Cyg X-1 (Orosz et al. 2011). Unlike LMC X-3's secondary, the companion stars in these systems do not fill their Roche lobes, and therefore the ellipsoidal light curves by themselves are much less constraining. Fortunately, for these systems the radius of the companion star can be found from the distance, the apparent magnitude, the extinction, the effective temperature of the star, and the bolometric correction determined from model atmospheres. The independently derived stellar radius in turn serves to strongly constrain the available parameter space for the dynamical model.

By virtue of its membership in the LMC (e.g. see Cowley et al. 1983), the distance to LMC X-3 is likewise well determined, and we adopt a distance modulus of $18.41 \pm 0.10 \text{ mag}$ as documented in the Supplementary Information of Orosz et al. (2007). However, given the erratic optical variability that is added to the underlying ellipsoidal modulation and the presence of light from the accretion disk, it is hard to define a baseline appar-

ent magnitude for LMC X-3. Instead we take a different approach. For a fixed apparent V magnitude, we can compute what the radius of a spherical star would have to be at the distance of the LMC given a temperature, extinction, a bolometric correction, and a correction for light from the accretion disk. For this exercise we used a V -band extinction of $A_V = 0.223 \pm 0.030$ based on the column density of $N_H = (3.8 \pm 0.8) \times 10^{20} \text{ cm}^{-2}$ (Page et al. 2003) and the conversion from N_H to A_V given by Predehl & Schmitt (1995). The bolometric corrections were interpolated from the BSTAR 2006 grid given by Lanz & Hubeny (2007). We assume the star contributes $85 \pm 5\%$ of the V -band light. Using these assumptions, we computed the radius and its uncertainty for a range of apparent V magnitudes for an effective temperature of $T_{\text{eff}} = 15,000 \pm 100 \text{ K}$ and for $T_{\text{eff}} = 15,500 \pm 100 \text{ K}$. The results are shown in Figure 15.

For a fixed V magnitude, the formal uncertainty in the computed radius is between about 0.2 and $0.3 R_\odot$, compared to the uncertainty of $0.24 R_\odot$ from the dynamical model. The 1σ regions of the model radius (shown as the horizontal dotted lines in Figure 15) and the radius from the distance overlap for $17.05 \lesssim V \lesssim 17.30$ when $T_{\text{eff}} = 15,000 \text{ K}$ and $16.95 \lesssim V \lesssim 17.20$ when $T_{\text{eff}} = 15,500 \text{ K}$, with the best matches occurring for $V \approx 17.15$ at $T_{\text{eff}} = 15,000 \text{ K}$ and $V \approx 17.10$ at $T_{\text{eff}} = 15,500 \text{ K}$.

This range of V magnitude for the star is in good agreement with the minimum V magnitude that we infer for LMC X-3 in two ways using the well-calibrated SMARTS data: (1) For the “X-quartered” data for which X-ray heating is minimal, the apparent V magnitude is 17.1 at the minimum at phase 0.5 and 16.95 at the maximum at phase 0.25; a spherical star with a radius equal to the effective radius of the companion star would have $V = 17.02$. (2) Focusing on the anomalous low state of 2008 December 11 – 2009 June 17 reported by Smale & Boyd (2012), and allowing for the two-week lag in X-ray intensity, the mean and standard deviation for 24 consecutive, near-nightly SMARTS observations is $V = 17.05 \pm 0.08$. Adopting as our minimum $V = 17.05$ and allowing for a 1% uncertainty in the zero-point, the vertical dotted lines in Figure 15 show the 1σ range of the apparent V magnitude of the system. The vertical and horizontal dotted lines form a box in the V - R_2

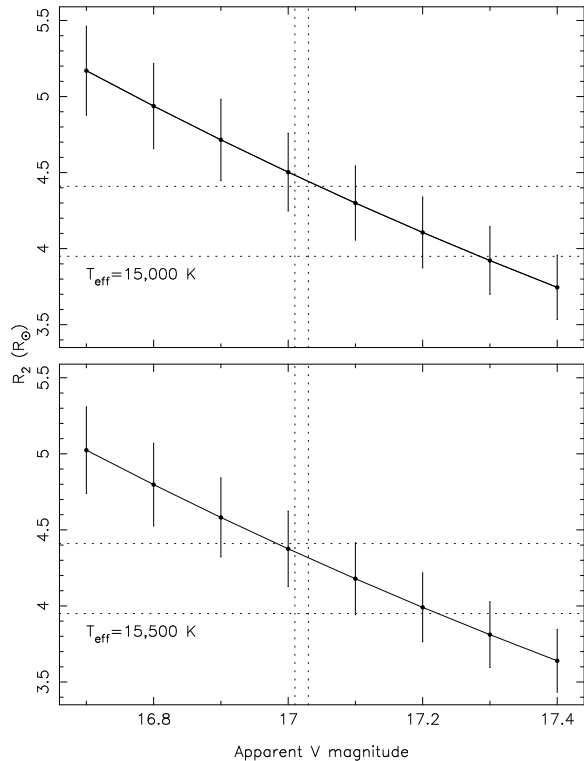


Fig. 15.— The computed radius of the secondary star as a function of the apparent V magnitude assuming an effective temperature of $T_{\text{eff}} = 15,000 \pm 100 \text{ K}$ (top) and $T_{\text{eff}} = 15,500 \pm 100 \text{ K}$ (bottom). We assume a distance modulus of 18.41 ± 0.10 , an extinction of $A_V = 0.223 \pm 0.030$, and a disk fraction of 0.15 ± 0.05 . The horizontal dotted lines denote the 1σ range in the radius found from the dynamical model, and the vertical dotted lines denote the 1σ range of apparent V magnitude of the system when the accretion disk light is minimal.

plane, and the curve defining the computed radius as a function of the distance passes through this box when $T_{\text{eff}} = 15,500 \text{ K}$ and passes very close when $T_{\text{eff}} = 15,000 \text{ K}$.

There are claims that LMC X-3 is at times fainter by a few tenths of a magnitude than our adopted minimum of $V = 17.05 \text{ mag}$ (Van der Klis et al. 1983; Soria et al. 2001; Brocksopp et al. 2001). However, the V -band zero point is much less secure for the data considered in this earlier work than for our SMARTS data, where it was determined via standard star observations on 44 photometric nights. Furthermore, it seems un-

likely that LMC X-3 was actually fainter in these earlier observations given that our determination was made during an extreme low state (Smale and Boyd 2012).

Thus, to summarize, the radius of the star computed using the distance, temperature, apparent magnitude, and extinction is fully consistent with the radius found from the dynamical model when $T_{\text{eff}} = 15,500$ K and is well within the 1σ uncertainty when $T_{\text{eff}} = 15,000$ K. The strong consistency in the radius derived from the two different methods is reassuring and gives us extra confidence in our dynamical model.

6. Discussion and Conclusions

Our mass for the black hole of $6.98 \pm 0.56 M_{\odot}$ is considerably more precise than earlier estimates for three principal reasons: First, we have far more radial velocity data of high quality for the secondary star, which yield a much improved determination of its K -velocity. Second, we have obtained the first accurate measurement of the projected rotational velocity of the secondary, which is an important constraint on the dynamical model. Third, we have analyzed a much larger body of ellipsoidal light curve data than any previous study (e.g., Kuiper et al. 1988).

In their pioneering work on LMC X-3, Cowley et al. (1983) concluded that the most plausible mass of the black hole was $\sim 9 M_{\odot}$ with a lower limit of $M > 7 M_{\odot}$. To reach this conclusion, Cowley et al. had to assume a mass for the secondary star. Based on their spectral classification of the star as B3V, they deduced its mass to be $4 - 8 M_{\odot}$, greater than our value of $M_2 = 3.63 \pm 0.57 M_{\odot}$. Estimating the mass based on the spectral type is problematic for a star that has lost an indeterminate amount of mass. On a related note, our measurement of the surface gravity of the star, $\log g = 3.740 \pm 0.020$, shows that it matches more closely the gravity of a giant (class III) than the gravity of a main sequence star (class V). For example, the nominal masses and radii for a B3V/B5V star given by Ostlie & Carroll (1996) correspond to surface gravities of $\log g = 4.07/3.98$, while their surface gravity for a B5III star is $\log g = 3.68$.

Soria et al. (2001) and Val-Baker et al. (2007) provided mass estimates after making corrections

to the K -velocity of the secondary star to account for X-ray heating. Based on the system colors as measured by the Optical Monitor on *XMM-Newton*, Soria et al. concluded that the secondary star is a B5 subgiant that fills its Roche lobe. Using an evolutionary model they determined a mass of $M_2 = 4.7 M_{\odot}$ for the secondary star. Next, Soria et al. applied a K -correction of $\Delta K = -30 \pm 5$ km s $^{-1}$ to the K -velocity from Cowley et al. (1983) to arrive at the “true” K -velocity of 205 ± 12 km s $^{-1}$. The sign of their K -correction is negative because Soria et al. used the procedure that assumes heating by “soft” X-ray photons (Section 5.2.2). Finally, Soria et al. used their secondary star mass and corrected K -velocity to arrive at their lower limit of $M > 5.8 \pm 0.6 M_{\odot}$.

Val-Baker et al. (2007) measured a K -velocity of $K_2 = 242.4 \pm 4.3$ km s $^{-1}$ from the five UVES spectra. Their K -correction of 14.3 km s $^{-1}$ is positive because they used the procedure that assumes irradiation by “hard” photons; their adopted K -velocity is therefore $K_2 = 256.7 \pm 4.9$ km s $^{-1}$. By comparing their spectra to standard star spectra, Val-Baker et al. determined a spectral type of B3V at phase 0.22 when X-ray heating is significant, and B5V at phase 0.86, when X-ray heating is slight. Converting these spectral types into temperatures using Kurucz models, they arrived at effective temperatures of $15,400$ K for the unheated face and $18,700$ K for the heated face. This temperature change was used to then find their K -correction. Finally, after adopting a nominal mass of $5.9 M_{\odot}$ for a B5V star (e.g. Ostlie & Carroll 1996), Val-Baker found a mass range for the black hole of $9.5 \leq M \leq 13.6 M_{\odot}$.

Soria et al. (2001) and Val-Baker et al. (2007) not only disagree by a factor of two on the magnitude of the K -correction, they even disagree on its sign. As noted earlier, the disagreement on the sign of the effect results from Soria et al. assuming that the X-ray spectrum illuminating the star is soft, while Val-Baker et al. assumed it is hard. Setting aside the difference in the signs for the moment, we believe that the magnitudes of these corrections are too large [where $|\Delta K| = 30$ km s $^{-1}$ for Soria et al. (2001) and $|\Delta K| = 14.3$ km s $^{-1}$ for Val-Baker et al. (2007)]. In contrast, consideration of our much more extensive data set shows that X-ray heating has a modest effect on the K -velocity (Section 4.1), which is probably because

the star is shielded by the outer part of the accretion disk and because the X-ray emitting region has a disk-like geometry. Val-Baker et al. inferred a temperature difference of 3300 K between the heated and unheated faces of the star. However, as shown in Figure 8, we measure a temperature range of less than half their value. The result of Val-Baker et al. is subject to the complication that the X-ray luminosity of the system (as measured by the *RXTE* ASM) varied by a factor of two over the course of their UVES observations (see Table 2). Because the K -correction is strongly supralinear with temperature, our correction for 1500 K is much smaller than that of Val-Baker et al. for 3300K.

The black hole mass of $6.98 \pm 0.56 M_{\odot}$ is entirely consistent with the masses of black hole in transient systems with low-mass secondaries ($7.8 \pm 1.2 M_{\odot}$; Özel et al. 2010; Farr et al. 2011). In contrast, the black hole masses in the persistently-bright, wind-fed systems with high mass secondaries (e.g. M33 X-7, LMC X-1, and Cyg X-1) are considerably larger (Orosz et al. 2007, 2009, 2011). Considering the mass of the black hole and the following three other properties of LMC X-3, we classify the system as a member of the transient black hole binaries that are fed by Roche-lobe overflow, rather than as a member of the persistent systems whose black holes are wind-fed by massive O-type or Wolf-Rayet secondaries (McClintock et al. 2013): (1) Mass transfer via Roche-lobe overflow is expected given the mass ratio reported herein ($M/M_2 \approx 2$). (2) Although normally X-ray bright, LMC X-3 is highly variable and on occasion enters a prolonged low-intensity state that is dominated by a hard power-law component (Wilms et al. 2001; Smale & Boyd 2012). (3) Likewise, the low spin of the black hole (Davis et al. 2006; Steiner et al. 2014) distinguishes LMC X-3 from the persistent black holes and is consistent with that of other transient black holes (McClintock et al. 2013).

One obvious difference between LMC X-3 and a typical transient system like A0620-00 is that LMC X-3 has never been reported to be in a true X-ray quiescent state with $L_x \lesssim 10^{33}$ ergs s $^{-1}$. The mass transfer rate in LMC X-3 is high compared to a typical transient because the relatively massive secondary is presumably evolving on a nuclear timescale. The higher mass transfer rate re-

sults in much shorter recurrence timescales, according to the disk instability model (Cannizzo, Chen, & Livio 1995; Lasota 2001). In the context of this model, perhaps the recurrence time is so short that LMC X-3 is perpetually in an outburst state.

Finally, although a detailed evolutionary model is beyond the scope of this paper, we briefly speculate on the future of LMC X-3. Since the present-day mass of the secondary star is less than that of the black hole, the mass transfer is expected to be both thermally and dynamically stable (Tauris & van den Heuvel 2006). Mass transfer from the lower mass object to the higher mass object results in an expansion of the orbit (e.g., the period and the separation both increase). The secondary star’s radius would also increase, as it continues to fill its Roche lobe. The mass that is transferred through the accretion disk will tend to increase the spin of the black hole. By the time core H-burning ceases, the star may have transferred a considerable amount of its current mass to the black hole. Thus, it appears that LMC X-3, will end up with a relatively massive black hole, a long orbital period, appreciable spin, and a low mass companion. This future version of LMC X-3 will likely bridge the gap between most transient systems and the extreme system GRS 1915+105 (McClintock et al. 2006; Steeghs et al. 2013).

JFS was supported by NASA Hubble Fellowship grant HST-HF-51315.01. The work of JEM was supported in part by NASA grant NNX11AD08G. DS acknowledges a STFC Advanced Fellowship as well as support through the NASA Guest Observer Program. MMB and CDB acknowledge support from the National Science Foundation via the grants AST 0407063 and AST 070707.

A. Conversion of *RXTE* ASM fluxes to X-ray Luminosities

To convert a measurement of the 2-12 keV X-ray intensity from the *RXTE* All Sky Monitor (ASM) into an estimate of the bolometric X-ray luminosity, the following procedure was used. First, the *RXTE* ASM count rate was converted into a Crab-unit equivalent intensity, and subsequently into a flux using the 2-12 keV brightness of the Crab, which is a commonly employed flux conversion method. Each flux measurement was then converted to an X-ray luminosity using $L_x(\text{erg s}^{-1}) = (\text{ASM rate}) \times (8.85 \times 10^{37})$, assuming isotropic emission and a distance of $d = 48.1$ kpc. We do not use a particular model in making this conversion and in deriving the bolometric correction; rather, we take the following approach:

1) We consider fits to typical low-and-high luminosity *RXTE* PCA spectra of LMC X-3 consisting of a disk and power-law (`simpl × Kerrbb`; see Steiner et al. 2010). We find that the model-extrapolated bolometric (10 eV – 100 keV) flux is typically two to three times larger than the 2-12 keV flux, with a bolometric conversion factor of 2.5 being a good and representative value.

2) We have estimated the error induced from having computed fluxes based upon the spectral shape of the Crab. Specifically, we checked limiting cases in which LMC X-3s spectrum is assumed to be i) a pure blackbody and ii) a pure power-law. In the first instance, for characteristic temperatures between 0.1-1.0 keV, we find that our conversion *overestimates* the X-ray flux by 10 to 20%. In the second instance, we examine spectral indexes ranging from 2.0-2.7 (see Steiner et al. 2010), and find that the flux error is $\lesssim 10\%$. These errors are commensurate with our typical count rate uncertainties, which are $\sim 20\%$, indicating that although a bias may be present, it would manifest at the $\sim 1\sigma$ level. Furthermore, we note that since we do not have the instantaneous X-ray spectral information on the system which would enable a precise flux estimate, any different model-based approach would be subject to comparable systematic uncertainties, but it would also be more convoluted than our present approach, which has the virtue of being simple and easily reproduced.

REFERENCES

- Bernstein, R., Sheckman, S., Gunnels, S., Mochmacki, S., & Athey, A. 2002, *Proc. SPIE* 4841, 1694
- Brocksopp, C., Groot, P. J., & Wilms, J. 2001, *MNRAS*, 328, 139
- Cannizzo, J. K., Chen, W., & Livio, M. 1995, *ApJ*, 454, 880
- Charbonneau, P. 1995, *ApJS*, 101, 309
- Charles, P. A., & Coe, M. J. 1995, in *X-ray Binaries*, eds. W. H. G. Lewin, J. van Paradijs, & E. P. J. van den Heuvel, (Cambridge: Cambridge University Press)
- Cowley, A. P., Crampton, D., Hutchings, J. B., Remillard, R., & Penfold, J. E. 1983, *ApJ*, 272, 118
- Cowley, A. P., Schmidtke, P. C., Ebisawa, K., Makino, F., Remillard, R. A., Crampton, D., Hutchings, J. B., Kitamoto, S., & Treves, A. 1991, *ApJ*, 381, 526
- Davis, S. W., Done, C., & Blaes, O. M. 2006, *ApJ*, 647, 525
- Eggleton, P. P. 1983, *ApJ*, 268, 368
- Gies, D. R., & Bolton, C. T. 1986, *ApJ*, 304, 371
- Güver, T., & Özel, F. 2009, *MNRAS*, 400, 2050
- Hubeny, I. 1998, *Computer Physics Comm.*, 52, 103
- Hubeny, I., Stefl, S., & Harmanec, P. 1985, *Bull. Astron. Inst. Czechosl.* 36, 214
- Kalogera, V. & Baym, G. 1996, *ApJ*, 470, L61
- Kubota, A., Done, C., Davis, S. W., Dotani, T., Mizuno, T., & Ueda, Y. 2010, *ApJ* 714, 860
- Kuiper, L., van Paradijs, J., & van der Klis, M. 1988, *A&A*, 203, 79
- Landolt, A. U. 1992, *AJ*, 104, 340
- Lanz, T., & Hubeny, I. 2007, *ApJS*, 169, 83
- Lasota, J.-P. 2001, *NewAR*, 45, 449L
- Leong, C. Kellogg, E., Gursky, H., Tananbaum, H., & Giacconi, R. 1971, *ApJ*, 170, L67
- Marsh, T. R., Robinson, E. L., & Wood, J. H. 1994, *MNRAS*, 266, 137
- McClintock, J. E., Shafee, R., Narayan, R., Remillard, R. A., Davis, S. W., & Li, L., 2006, *ApJ*, 652, 518
- Orosz, J. A., & Hauschildt, P. H. 2000, *A&A*, 364, 265
- Orosz, J. A., McClintock, J. E., Narayan, R., Bailyn, C. D., Macri, L., Liu, J., Pietsch, W., Remillard, R. A., Shporer, A., & Mazeh, T. 2007, *Nature*, 449, 872
- Orosz, J. A., Steeghs, D., McClintock, J. E., Torres, M. A. P., Bochkov, I., et al. 2009, *ApJ*, 697, 573
- Orosz, J. A., McClintock, J. E., Aufdenberg, J. P., Remillard, R. A., Reid, M. J., Narayan, R., & Gou, L. 2011, *ApJ*, 742, 84
- Ostlie, D. A., & Carroll, B. W. (ed.) 1996, *An Introduction to Modern Stellar Astrophysics* (New York: Addison-Wesley)
- Özel, F., Psaltis, D., Narayan, R., & McClintock, J. E. 2010, *ApJ*, 725, 1918
- Page, M. J., Soria, R., Wu, K., Mason, K. O., Cordova, F. A., & Priedhorsky, W. C. 2003, *MNRAS*, 345, 649
- Persson, S. E., Murphy, D. C., Krzeminski, W., Roth, M., & Rieke, M. J. 1998, *AJ*, 116, 2475
- Phillips, S. N., Shahbaz, T., & Podsiadlowski, Ph. 1999, *MNRAS*, 304, 839
- Predehl, P., & Schmitt, J. H. M. M. 1995, *A&A*, 293, 889
- Song, L., Tripp, T. M., Wang, Q. D., Yao, Y., Cui, W., et al. 2010, *AJ*, 140, 794
- Soria, R., Wu, K., Page, M. J., & Sakelliou, I. 2001, *A&A*, 365, L273
- Smale, A. P., & Boyd, P. T. 2012, *ApJ*, 756, 146
- Steeghs, D., McClintock, J. E., Parsons, S. G., Reid, M. J., Littlefair, S., & Dhillon, V. S. 2013, *ApJ*, 768, 185

- Steiner, J. F., McClintock, J. E., Remillard, R. A., Gou, L., Yamada, S., & Narayan, R. 2010, *ApJ*, 718, L117
- Steiner, J. F., McClintock, J. E., Orosz, J. A., Buxton, M. M., Bailyn, C. D., Remillard, R. A., & Kara, E. 2013, *ApJ*, submitted
- Steiner, J. F., McClintock, J. E., Orosz, J. A., Remillard, R. A., Bailyn, C. D., Kolehmainen, M., & Straub, O. 2014, *ApJ*, submitted
- Straub, O., Burs, M., Sądowski, A., Steiner, J. F., Abramowicz, M. A., Kluźniak, W., McClintock, J. E., Narayan, R., & Remillard, R. A., 2011, *A&A*, 533, A67
- Tauris, T. M., & van den Heuvel, E. P. J. 2006, in *Compact Stellar X-ray Sources*, ed. W. H. G. Lewin & M. van der Klis (Cambridge: Cambridge Univ. Press), arXiv:astro-ph/0303456
- Tegmark, X., Strauss, M. A., Blanton, M. R., Abazajian, K., Dodelson, S., et al. 2004, *Phys. Rev. D*, 69, 103501
- Ter Braak, C. J. F. 2006, *Stat. Comput.* 16, 239
- Tonry, J., & Davis, M. 1979, *AJ*, 84, 1511
- Val-Baker, A. K. F., Norton, A. J., & Negueruela, I. 2007, *AIP Conference Proceedings*, Vol. 924, pp. 530-533
- van der Klis, M. 1983, *A&A*, 126, 265
- van der Klis, M., Clausen, J. V., Jensen, K., Tjemkes, S., & van Paradijs, J. 1985, *A&A*, 151, 322
- van Paradijs, J., & McClintock, J. E. 1995, in *X-ray Binaries*, eds. W. H. G. Lewin, J. van Paradijs, & E. P. J. van den Heuvel, (Cambridge: Cambridge University Press)
- Warren, P. R., & Penfold, J. E. 1975, *MNRAS*, 172, 41P
- Wilms, J., Nowak, M. A., Pottschmidt, K., Heindl, W. A., Dove, J. B., & Begelman, M. C. 2001, *MNRAS*, 320, 327
- Wilson, R. E., & Sofia, S. 1976, *ApJ*, 203, 182
- Wilson, R. E. 1990, *ApJ*, 356, 613
- Zhang, E.-H., Robinson, E. L., & Nather, R. E. 1986, *ApJ*, 305, 740

TABLE 2
STELLAR PARAMETERS FROM SPECTRA OF LMC X-3

UT date (YYYY-MM-DD)	HJD (+2,450,000)	phase	ASM ^a ct s ⁻¹	T _{eff} (K)	log g (cgs)	V _{rot} sin i (km s ⁻¹)	k
UVES Spectra							
2004-12-19	3358.56490	0.860	1.82 ± 0.42	15,400 ± 47	3.695 ± 0.030	97.8 ± 3.3	0.797 ± 0.001
2005-01-04	3374.72113	0.336	1.89 ± 0.15	16,750 ± 120	3.792 ± 0.032	119.9 ± 4.4	0.769 ± 0.003
2005-01-08	3378.63666	0.633	1.87 ± 0.30	16,541 ± 133	3.868 ± 0.008	111.0 ± 4.1	0.755 ± 0.003
2005-03-19	3448.52084	0.626	3.15 ± 0.18	16,682 ± 127	3.812 ± 0.036	120.9 ± 4.0	0.676 ± 0.002
2005-03-20	3449.53491	0.220	3.14 ± 0.54	16,326 ± 96	3.784 ± 0.031	143.1 ± 2.9	0.747 ± 0.003
...	16,435 ± 60 ^b	3.801 ± 0.010 ^b	121.4 ± 1.4 ^b	0.732 ± 0.001 ^b
MIKE Spectra							
2005-01-20	3390.74244	0.734	1.93 ± 0.53	16,211 ± 80	3.541 ± 0.009	131.7 ± 4.3	0.720 ± 0.004
2005-01-20	3390.77549	0.754	1.94 ± 0.54	15,882 ± 105	3.685 ± 0.030	118.3 ± 7.0	0.724 ± 0.004
2005-01-21	3391.68953	0.290	1.96 ± 0.65	15,992 ± 184	2.885 ± 0.018	158.7 ± 6.1	0.702 ± 0.009
2005-01-22	3392.77873	0.929	1.99 ± 0.53	15,220 ± 180	3.481 ± 0.050	100.8 ± 10.7	0.609 ± 0.006
2005-01-24	3394.69509	0.053	2.03 ± 0.37	15,722 ± 327	2.985 ± 0.030	190.4 ± 6.9	0.721 ± 0.015
2005-01-25	3395.73754	0.664	2.08 ± 0.55	16,278 ± 321	3.427 ± 0.014	141.9 ± 7.6	0.711 ± 0.008
...	15,781 ± 61 ^b	3.319 ± 0.004 ^b	132.6 ± 2.9 ^b	0.664 ± 0.002 ^b
2007-12-20	4454.58242	0.757	0.85 ± 0.31	15,762 ± 104	3.692 ± 0.024	121.4 ± 4.4	0.873 ± 0.003
2007-12-20	4454.60559	0.771	0.85 ± 0.31	15,964 ± 43	3.862 ± 0.020	121.3 ± 4.7	0.875 ± 0.001
2007-12-20	4454.62818	0.784	0.85 ± 0.31	15,440 ± 60	3.650 ± 0.014	123.3 ± 5.1	0.853 ± 0.002
2007-12-20	4454.65045	0.797	0.85 ± 0.31	15,635 ± 95	3.775 ± 0.027	117.3 ± 5.1	0.882 ± 0.002
2007-12-20	4454.68433	0.817	0.85 ± 0.31	15,497 ± 154	3.777 ± 0.028	118.2 ± 4.2	0.863 ± 0.005
2007-12-20	4454.70568	0.829	0.85 ± 0.31	15,418 ± 109	3.751 ± 0.016	116.7 ± 3.2	0.860 ± 0.003
2007-12-20	4454.72792	0.843	0.85 ± 0.31	15,207 ± 71	3.692 ± 0.015	108.7 ± 3.3	0.867 ± 0.002
2007-12-20	4454.75014	0.856	0.85 ± 0.31	15,398 ± 115	3.710 ± 0.023	113.7 ± 4.9	0.884 ± 0.003
2007-12-20	4454.77178	0.868	0.85 ± 0.31	15,090 ± 115	3.580 ± 0.023	123.6 ± 3.8	0.879 ± 0.004
2007-12-20	4454.79457	0.882	0.85 ± 0.31	15,381 ± 76	3.655 ± 0.021	111.0 ± 3.6	0.873 ± 0.003
2007-12-20	4454.81744	0.895	0.85 ± 0.31	15,207 ± 71	3.721 ± 0.021	107.7 ± 3.8	0.872 ± 0.002
2007-12-20	4454.83678	0.906	0.85 ± 0.31	15,018 ± 151	3.584 ± 0.024	117.2 ± 6.4	0.897 ± 0.006
...	15,415 ± 34 ^b	3.365 ± 0.014 ^b	114.0 ± 2.6 ^b	0.798 ± 0.002 ^b
2007-12-21 ^c	4455.56375	0.333	0.86 ± 0.78
2007-12-21 ^c	4455.58585	0.346	0.86 ± 0.78
2007-12-21 ^c	4455.63073	0.372	0.86 ± 0.78
2007-12-21	4455.65994	0.389	0.86 ± 0.70	15,872 ± 120	3.247 ± 0.022	114.4 ± 4.9	0.914 ± 0.007
2007-12-21	4455.68207	0.402	0.86 ± 0.70	16,048 ± 151	3.294 ± 0.025	120.8 ± 5.1	0.885 ± 0.006
2007-12-21	4455.70422	0.415	0.86 ± 0.70	16,164 ± 235	3.239 ± 0.032	111.4 ± 7.6	0.886 ± 0.011
2007-12-21	4455.72745	0.429	0.86 ± 0.70	15,817 ± 160	3.322 ± 0.020	107.1 ± 4.1	0.851 ± 0.005
2007-12-21	4455.74956	0.442	0.86 ± 0.70	16,114 ± 139	3.287 ± 0.017	106.9 ± 5.9	0.815 ± 0.006
2007-12-21	4455.77165	0.455	0.86 ± 0.70	16,498 ± 203	3.288 ± 0.024	116.8 ± 4.9	0.837 ± 0.007
2007-12-21	4455.79313	0.467	0.86 ± 0.70	16,984 ± 141	3.391 ± 0.020	117.2 ± 3.3	0.805 ± 0.005
2007-12-21	4455.81523	0.480	0.86 ± 0.70	16,825 ± 145	3.436 ± 0.023	130.1 ± 5.2	0.824 ± 0.006
2007-12-21	4455.83735	0.493	0.86 ± 0.70	15,958 ± 233	3.356 ± 0.041	114.5 ± 4.9	0.836 ± 0.007
...	18,085 ± 93 ^b	3.297 ± 0.009 ^b	120.2 ± 2.2 ^b	0.800 ± 0.004 ^b
2008-02-27	4523.54114	0.207	2.21 ± 0.63	15,498 ± 85	3.000 ± 0.015	167.7 ± 11.2	0.766 ± 0.009
2008-02-27	4523.56408	0.220	2.21 ± 0.63	15,399 ± 249	2.984 ± 0.018	184.5 ± 6.7	0.769 ± 0.013
2008-02-27	4523.58682	0.233	2.21 ± 0.63	15,399 ± 55	2.984 ± 0.006	184.5 ± 2.5	0.747 ± 0.003
2008-02-27	4523.60952	0.247	2.21 ± 0.63	15,717 ± 146	2.898 ± 0.058	193.0 ± 2.7	0.785 ± 0.012
2008-02-27	4523.63193	0.260	2.21 ± 0.63	15,704 ± 151	2.955 ± 0.057	188.2 ± 6.8	0.760 ± 0.007
2008-02-27	4523.67602	0.286	2.21 ± 0.63	15,653 ± 353	3.048 ± 0.055	162.9 ± 8.7	0.797 ± 0.017
...	17,003 ± 21 ^b	3.415 ± 0.007 ^b	160.3 ± 2.3 ^b	0.717 ± 0.002 ^b
2008-02-28	4524.53912	0.792	2.24 ± 0.39	16,302 ± 122	3.793 ± 0.020	111.3 ± 5.3	0.736 ± 0.003
2008-02-28	4524.56150	0.805	2.24 ± 0.39	15,677 ± 145	3.681 ± 0.025	121.4 ± 6.6	0.723 ± 0.006
2008-02-28	4524.58384	0.818	2.24 ± 0.39	15,357 ± 116	3.801 ± 0.024	100.9 ± 5.2	0.720 ± 0.004
2008-02-28	4524.60626	0.831	2.24 ± 0.39	15,895 ± 84	3.849 ± 0.023	94.9 ± 4.6	0.731 ± 0.004
2008-02-28	4524.62862	0.845	2.24 ± 0.39	15,808 ± 62	3.630 ± 0.020	103.9 ± 3.5	0.705 ± 0.002
2008-02-28	4524.65381	0.859	2.24 ± 0.39	15,727 ± 115	3.522 ± 0.021	108.0 ± 3.7	0.693 ± 0.004
...	16,094 ± 71 ^b	3.435 ± 0.010 ^b	106.3 ± 2.1 ^b	0.661 ± 0.002 ^b
2008-02-29	4525.53557	0.377	2.22 ± 0.44	16,536 ± 173	3.245 ± 0.021	118.0 ± 3.4	0.641 ± 0.005
2008-02-29	4525.55787	0.390	2.22 ± 0.44	16,650 ± 195	3.400 ± 0.020	108.9 ± 6.8	0.634 ± 0.006

TABLE 2—*Continued*

UT date (YYYY-MM-DD)	HJD (+2,450,000)	phase	ASM ^a ct s ⁻¹	T_{eff} (K)	log g (cgs)	$V_{\text{rot}} \sin i$ (km s ⁻¹)	k
2008-02-29	4525.58156	0.406	2.22 ± 0.44	$16,595 \pm 128$	3.417 ± 0.026	106.2 ± 5.3	0.618 ± 0.004
2008-02-29	4525.60393	0.417	2.22 ± 0.44	$16,850 \pm 150$	3.297 ± 0.027	118.0 ± 4.3	0.624 ± 0.004
2008-02-29	4525.62682	0.431	2.22 ± 0.44	$16,650 \pm 85$	3.383 ± 0.025	114.9 ± 3.3	0.617 ± 0.002
...	$18,352 \pm 73^{\text{b}}$	$3.522 \pm 0.022^{\text{b}}$	$107.6 \pm 1.7^{\text{b}}$	$0.565 \pm 0.003^{\text{b}}$
2008-03-01	4526.52329	0.956	2.20 ± 0.19	$15,996 \pm 69$	3.482 ± 0.018	122.4 ± 3.5	0.677 ± 0.002
2008-03-01	4526.54550	0.969	2.20 ± 0.19	$15,440 \pm 98$	3.600 ± 0.017	120.3 ± 3.9	0.707 ± 0.003
2008-03-01	4526.56776	0.982	2.20 ± 0.19	$15,653 \pm 124$	3.488 ± 0.032	147.0 ± 11.9	0.722 ± 0.007
2008-03-01	4526.59005	0.995	2.20 ± 0.19	$15,545 \pm 205$	3.501 ± 0.023	126.6 ± 5.5	0.722 ± 0.005
2008-03-01	4526.61241	0.008	2.20 ± 0.19	$15,475 \pm 107$	3.455 ± 0.020	140.3 ± 5.3	0.720 ± 0.004
2008-03-01	4526.63475	0.021	2.20 ± 0.19	$15,461 \pm 87$	3.414 ± 0.021	125.3 ± 3.9	0.703 ± 0.003
2008-03-01	4526.65820	0.035	2.20 ± 0.19	$15,168 \pm 54$	3.333 ± 0.007	139.3 ± 7.4	0.680 ± 0.002
...	$16,106 \pm 105^{\text{b}}$	$3.241 \pm 0.011^{\text{b}}$	$125.0 \pm 2.4^{\text{b}}$	$0.634 \pm 0.003^{\text{b}}$

^aX-ray intensity from the *RXTE* All Sky Monitor.

^bDerived from averaged spectrum.

^cContaminated by Balmer emission.

TABLE 5
ELC MODEL FITS

Parameter	A93	A93	W94	W94	W95	W95
	No heating	X-ray heating	No heating	X-ray heating	No heating	X-ray heating
i (deg)	71.58 ± 0.12	72.29 ± 0.42	64.62 ± 5.49	62.88 ± 4.40	69.18 ± 0.65	67.43 ± 1.27
$\log(L_x/\text{erg s}^{-1})$...	37.75 ± 0.13	...	38.50 ± 0.07	...	38.06 ± 0.44
K_2 (km s $^{-1}$)	242.02 ± 2.75	241.00 ± 1.20	241.11 ± 2.14	240.95 ± 3.00	241.21 ± 3.00	241.06 ± 2.02
Q	2.31 ± 0.08	1.93 ± 0.15	1.93 ± 0.23	1.93 ± 0.24	1.97 ± 0.16	1.92 ± 0.16
$\Delta\phi$	0.00084 ± 0.00152	0.00347 ± 0.00248	-0.04000 ± 0.00828	-0.02906 ± 0.00800	0.00046 ± 0.00273	-0.00309 ± 0.00679
$T_{\text{disk}}(K)$	42160.0 ± 13.8	36353.5 ± 10826.2	18423.7 ± 15045.5	22754.2 ± 7144.2	24395.1 ± 11113.9	17886.4 ± 2145.7
r_{out}	0.680 ± 0.054	0.400 ± 0.053	0.556 ± 0.269	0.694 ± 0.175	0.459 ± 0.064	0.503 ± 0.118
ξ	-0.0062 ± 0.0001	-0.1118 ± 0.0478	-0.0959 ± 0.0731	-0.0698 ± 0.0643	-0.1200 ± 0.0653	-0.0601 ± 0.0352
β (deg)	5.00 ± 0.51	4.53 ± 1.48	4.46 ± 3.29	2.84 ± 0.80	1.50 ± 2.01	3.37 ± 2.00
s_{spot}	1.10 ± 0.22	3.59 ± 1.87	5.25 ± 4.55	5.13 ± 4.54	2.24 ± 0.90	3.88 ± 5.34
θ_{spot} (deg)	30.02 ± 3.42	32.28 ± 6.61	208.32 ± 9.31	154.04 ± 4.28	185.84 ± 3.24	274.59 ± 122.15
r_{cut}	0.562 ± 0.067	0.844 ± 0.344	0.845 ± 0.344	0.617 ± 0.357	0.702 ± 0.267	0.874 ± 0.365
w_{spot} (deg)	12.43 ± 1.52	8.11 ± 4.96	3.29 ± 10.11	5.32 ± 4.59	49.75 ± 4.65	24.43 ± 24.85
B disk fraction	0.40 ± 0.02	0.20 ± 0.04	0.32 ± 0.17	0.37 ± 0.10	0.17 ± 0.10	0.25 ± 0.08
V disk fraction	0.51 ± 0.02	0.28 ± 0.05	0.18 ± 0.09	0.27 ± 0.10	0.15 ± 0.03	0.18 ± 0.03
M_2 (M_{\odot})	2.60 ± 0.15	3.41 ± 0.59	4.00 ± 1.03	4.18 ± 0.89	3.51 ± 0.45	3.80 ± 0.61
R_2 (R_{\odot})	3.80 ± 0.08	4.18 ± 0.24	4.41 ± 0.36	4.48 ± 0.31	4.22 ± 0.19	4.34 ± 0.24
$\log g_2$ (cgs)	3.69 ± 0.01	3.73 ± 0.02	3.75 ± 0.03	3.76 ± 0.03	3.73 ± 0.02	3.74 ± 0.02
M (M_{\odot})	6.02 ± 0.21	6.59 ± 0.29	7.73 ± 1.55	8.07 ± 1.52	6.91 ± 0.38	7.28 ± 0.47

TABLE 6
ELC MODEL FITS

Parameter	S96	S96	A96a	A96a	A96b	A96b
	No heating	X-ray heating	No heating	X-ray heating	No heating	X-ray heating
i (deg)	71.60 ± 2.47	70.46 ± 0.93	70.13 ± 1.04	67.84 ± 0.66	70.95 ± 2.51	70.63 ± 0.71
$\log(L_x/\text{erg s}^{-1})$...	38.21 ± 0.11	...	36.00 ± 1.18	...	36.03 ± 1.00
K_2 (km s $^{-1}$)	241.02 ± 3.01	241.01 ± 2.84	241.25 ± 1.68	241.22 ± 3.00	241.66 ± 3.44	241.10 ± 3.02
Q	1.90 ± 0.18	1.90 ± 0.16	2.06 ± 0.20	1.97 ± 0.11	1.98 ± 0.16	1.93 ± 0.17
$\Delta\phi$	-0.00890 ± 0.00575	-0.01511 ± 0.00480	-0.01010 ± 0.00534	-0.01800 ± 0.00307	-0.02351 ± 0.00391	0.00230 ± 0.00407
$T_{\text{disk}}(K)$	46687.8 ± 23161.4	49247.9 ± 2450.0	35888.8 ± 13316.2	41286.1 ± 7014.0	33577.9 ± 6930.0	37509.2 ± 3468.3
r_{out}	0.607 ± 0.066	0.730 ± 0.036	0.408 ± 0.217	0.740 ± 0.040	0.737 ± 0.161	0.633 ± 0.066
ξ	-0.1946 ± 0.0888	-0.2485 ± 0.0334	-0.1416 ± 0.0824	-0.1751 ± 0.0241	-0.2116 ± 0.0169	-0.1737 ± 0.0252
β (deg)	1.86 ± 2.71	1.62 ± 0.72	1.01 ± 0.15	2.57 ± 1.49	1.32 ± 0.78	1.51 ± 0.75
s_{spot}	1.66 ± 1.71	3.88 ± 1.82	2.00 ± 1.14	4.53 ± 4.45	3.34 ± 6.05	4.80 ± 4.45
θ_{spot} (deg)	190.14 ± 11.33	351.76 ± 7.95	185.79 ± 6.88	4.19 ± 3.20	144.24 ± 5.56	338.06 ± 7.79
r_{cut}	0.500 ± 0.488	0.618 ± 0.371	0.793 ± 0.228	0.724 ± 0.260	0.764 ± 0.261	0.615 ± 0.368
w_{spot} (deg)	47.43 ± 37.68	13.74 ± 19.70	49.91 ± 9.78	8.83 ± 2.80	21.61 ± 26.63	11.46 ± 23.27
B disk fraction	0.24 ± 0.07	0.30 ± 0.03	0.13 ± 0.11	0.36 ± 0.04	0.30 ± 0.09	0.25 ± 0.04
V disk fraction	0.25 ± 0.08	0.15 ± 0.02	0.15 ± 0.01	0.29 ± 0.03	0.15 ± 0.02	0.16 ± 0.02
M_2 (M_{\odot})	3.54 ± 0.49	3.62 ± 0.52	3.20 ± 0.59	3.61 ± 0.40	3.36 ± 0.57	3.53 ± 0.65
R_2 (R_{\odot})	4.24 ± 0.22	4.27 ± 0.23	4.09 ± 0.25	4.26 ± 0.16	4.16 ± 0.23	4.23 ± 0.29
$\log g_2$ (cgs)	3.73 ± 0.02	3.74 ± 0.02	3.72 ± 0.02	3.74 ± 0.01	3.73 ± 0.02	3.73 ± 0.03
M (M_{\odot})	6.74 ± 0.51	6.88 ± 0.44	6.59 ± 0.47	7.10 ± 0.42	6.68 ± 0.59	6.80 ± 0.40

TABLE 7
ELC MODEL FITS

Parameter	W96a	W96a	W96b	W96b	S98	S98
	No heating	X-ray heating	No heating	X-ray heating	No heating	X-ray heating
i (deg)	69.24 ± 1.83	69.17 ± 1.19	65.73 ± 1.22	63.71 ± 3.29	60.61 ± 6.21	63.61 ± 0.75
$\log(L_x/\text{erg s}^{-1})$...	37.64 ± 1.50	...	38.31 ± 1.62	...	38.05 ± 0.09
K_2 (km s $^{-1}$)	241.10 ± 2.92	241.08 ± 3.00	241.51 ± 3.17	240.71 ± 4.29	241.40 ± 1.91	241.01 ± 1.94
Q	1.93 ± 0.14	1.92 ± 0.16	1.83 ± 0.15	1.85 ± 0.43	2.02 ± 0.24	1.90 ± 0.13
$\Delta\phi$	-0.01546 ± 0.00502	-0.01626 ± 0.00640	0.02484 ± 0.01040	0.01864 ± 0.01523	-0.01059 ± 0.00676	-0.01363 ± 0.00391
$T_{\text{disk}}(K)$	39974.9 ± 10500.0	43156.5 ± 3500.1	46351.3 ± 913.3	28674.6 ± 20437.1	37757.6 ± 8943.4	41497.6 ± 26095.5
r_{out}	0.966 ± 0.073	0.921 ± 0.053	0.969 ± 0.052	0.932 ± 0.057	0.875 ± 0.387	0.746 ± 0.043
ξ	-0.2959 ± 0.0198	-0.3086 ± 0.0228	-0.0488 ± 0.0029	-0.0710 ± 0.0933	-0.1789 ± 0.1631	-0.2121 ± 0.1690
β (deg)	4.83 ± 3.01	5.00 ± 1.20	1.17 ± 1.10	4.55 ± 2.88	4.75 ± 3.24	4.99 ± 1.06
s_{spot}	5.91 ± 0.67	5.68 ± 0.86	3.34 ± 2.12	1.69 ± 5.21	0.80 ± 0.88	1.40 ± 0.22
θ_{spot} (deg)	191.15 ± 5.13	192.83 ± 6.51	332.44 ± 16.14	35.01 ± 322.31	21.11 ± 8.60	322.48 ± 10.27
r_{cut}	0.500 ± 0.197	0.506 ± 0.130	0.517 ± 0.206	0.869 ± 0.364	0.940 ± 0.433	0.629 ± 0.339
w_{spot} (deg)	25.76 ± 16.75	30.35 ± 7.08	25.97 ± 23.65	3.80 ± 46.18	48.70 ± 7.55	15.12 ± 13.87
B disk fraction	0.50 ± 0.07	0.49 ± 0.07	0.44 ± 0.02	0.51 ± 0.08	0.52 ± 0.29	0.43 ± 0.03
V disk fraction	0.18 ± 0.05	0.19 ± 0.03	0.69 ± 0.14	0.56 ± 0.12	0.38 ± 0.08	0.28 ± 0.04
M_2 (M_{\odot})	3.62 ± 0.43	3.64 ± 0.43	4.29 ± 0.59	4.39 ± 1.10	4.15 ± 0.35	4.21 ± 0.45
R_2 (R_{\odot})	4.27 ± 0.17	4.28 ± 0.17	4.53 ± 0.23	4.56 ± 0.43	4.46 ± 0.14	4.49 ± 0.17
$\log g_2$ (cgs)	3.74 ± 0.01	3.74 ± 0.02	3.76 ± 0.02	3.76 ± 0.04	3.76 ± 0.01	3.76 ± 0.01
M (M_{\odot})	6.99 ± 0.43	7.01 ± 0.39	7.86 ± 0.54	8.11 ± 1.30	8.39 ± 0.99	8.01 ± 0.36

TABLE 8
ELC MODEL FITS

Parameter	W98	W98	vdK	vdK	Halved	Halved
	No heating	X-ray heating	No heating	X-ray heating	No heating	X-ray heating
i (deg)	66.17 ± 1.86	63.34 ± 1.40	69.54 ± 0.46	69.80 ± 1.29	70.02 ± 0.40	69.79 ± 0.22
$\log(L_x/\text{erg s}^{-1})$...	38.13 ± 0.34	...	37.85 ± 0.26	...	37.60 ± 0.23
K_2 (km s $^{-1}$)	240.13 ± 2.85	241.04 ± 3.00	241.11 ± 2.96	241.03 ± 2.99	242.55 ± 1.93	239.55 ± 3.62
Q	1.98 ± 0.19	1.91 ± 0.24	1.94 ± 0.16	1.91 ± 0.16	2.24 ± 0.14	2.13 ± 0.10
$\Delta\phi$	-0.00145 ± 0.00285	-0.00195 ± 0.00523	0.02702 ± 0.00160	0.02704 ± 0.00232	-0.00073 ± 0.00070	-0.00294 ± 0.00402
$T_{\text{disk}}(K)$	20803.0 ± 5638.1	22031.7 ± 2540.2	30036.7 ± 7015.6	42288.4 ± 7365.4	30084.9 ± 172.8	27732.5 ± 12523.5
r_{out}	0.990 ± 0.026	0.990 ± 0.021	0.901 ± 0.039	0.912 ± 0.059	0.401 ± 0.000	0.405 ± 0.008
ξ	-0.1474 ± 0.0293	-0.1569 ± 0.0101	-0.1613 ± 0.0261	-0.1867 ± 0.1031	-0.1638 ± 0.0278	-0.1133 ± 0.0811
β (deg)	2.37 ± 2.16	3.69 ± 1.20	4.24 ± 1.02	2.14 ± 2.67	4.46 ± 2.32	2.25 ± 0.88
s_{spot}	1.81 ± 3.33	6.09 ± 1.31	1.27 ± 0.08	2.59 ± 1.07	1.36 ± 0.25	1.57 ± 0.57
θ_{spot} (deg)	191.88 ± 4.45	128.52 ± 46.82	178.71 ± 3.80	312.57 ± 307.65	173.81 ± 2.46	130.44 ± 47.40
r_{cut}	0.754 ± 0.236	0.749 ± 0.248	0.983 ± 0.260	0.639 ± 0.293	0.787 ± 0.203	0.708 ± 0.201
w_{spot} (deg)	49.21 ± 39.31	1.44 ± 45.45	49.14 ± 5.01	5.89 ± 43.42	50.00 ± 1.89	14.68 ± 19.01
B disk fraction	0.49 ± 0.07	0.52 ± 0.03	0.46 ± 0.03	0.41 ± 0.08	0.23 ± 0.06	0.17 ± 0.03
V disk fraction	0.19 ± 0.08	0.15 ± 0.03	0.28 ± 0.03	0.31 ± 0.03	0.16 ± 0.01	0.15 ± 0.00
M_2 (M_{\odot})	3.66 ± 0.72	4.22 ± 0.75	3.58 ± 0.43	3.64 ± 0.49	2.84 ± 0.35	2.97 ± 0.33
R_2 (R_{\odot})	4.28 ± 0.28	4.49 ± 0.30	4.25 ± 0.19	4.28 ± 0.21	3.92 ± 0.18	3.98 ± 0.15
$\log g_2$ (cgs)	3.74 ± 0.02	3.76 ± 0.03	3.73 ± 0.02	3.74 ± 0.02	3.70 ± 0.02	3.71 ± 0.01
M (M_{\odot})	7.24 ± 0.76	8.05 ± 0.61	6.93 ± 0.41	6.95 ± 0.44	6.36 ± 0.09	6.34 ± 0.33

TABLE 9
ELC MODEL FITS

Parameter	Quartered No heating	Quartered X-ray heating
i (deg)	69.52 ± 0.24	68.92 ± 0.61
$\log(L_x/\text{erg s}^{-1})$...	37.59 ± 0.87
K_2 (km s $^{-1}$)	241.20 ± 3.02	241.08 ± 3.00
Q	1.96 ± 0.04	1.93 ± 0.20
$\Delta\phi$	0.00614 ± 0.01014	0.01404 ± 0.01383
$T_{\text{disk}}(K)$	44931.6 ± 17.5	36366.6 ± 1520.0
r_{out}	0.400 ± 0.001	0.443 ± 0.130
ξ	-0.0785 ± 0.0037	-0.0163 ± 0.0030
β (deg)	1.98 ± 0.47	3.65 ± 2.34
s_{spot}	7.94 ± 0.89	1.84 ± 0.78
θ_{spot} (deg)	0.36 ± 6.84	326.49 ± 242.46
r_{cut}	0.575 ± 0.279	0.552 ± 0.435
w_{spot} (deg)	44.80 ± 12.10	8.96 ± 21.12
B disk fraction	0.15 ± 0.01	0.22 ± 0.04
V disk fraction	0.32 ± 0.02	0.21 ± 0.04
M_2 (M_{\odot})	3.51 ± 0.13	3.65 ± 0.47
R_2 (R_{\odot})	4.22 ± 0.05	4.28 ± 0.21
$\log g_2$ (cgs)	3.73 ± 0.01	3.74 ± 0.02
M (M_{\odot})	6.88 ± 0.25	7.03 ± 0.44